Nature Communications

https://doi.org/10.1038/s41467-026-72727-8

Article in Press

Breaking the catalysis-quenching dilemma in covalent organic frameworks with metal single-atom sites for enhanced electrochemiluminescence

Received: 28 August 2025

Accepted: 23 April 2026

Cite this article as: Wan, H., Du, Y., He, J. *et al.* Breaking the catalysis-quenching dilemma in covalent organic frameworks with metal single-atom sites for enhanced electrochemiluminescence. *Nat Commun* (2026). https://doi.org/10.1038/s41467-026-72727-8

Haifei Wan, Yuxin Du, Juan He, Yifei Chen, Jingshuai Li, Ying Qin, Ruimin Li, Liuyong Hu, Wenling Gu, Han Yu & Chengzhou Zhu

Breaking the Catalysis-Quenching Dilemma in Covalent Organic Frameworks with Metal Single-Atom Sites for Enhanced Electrochemiluminescence

Haifei Wan[1], Yuxin Du[1], Juan He[1], Yifei Chen[1], Jingshuai Li[1], Ying Qin[1], Ruimin Li[1], Liuyong Hu[2], Wenling Gu[1], Han Yu[3], and Chengzhou Zhu[1,*]

[1]State Key Laboratory of Green Pesticide, International Joint Research Center for Intelligent Biosensing Technology and Health, College of Chemistry, Central China Normal University, Wuhan 430079 (P. R. China).

[2]Hubei Key Laboratory of Plasma Chemistry and Advanced Materials, Hubei Engineering Technology Research Center of Optoelectronic and New Energy Materials, Wuhan Institute of Technology, Wuhan 430205 (P. R. China).

[3]Department of Applied Biology and Chemical Technology and Research Institute for Smart Energy, The Hong Kong Polytechnic University, Hung Hom, Hong Kong (P. R. China).

*Corresponding author: czzhu@ccnu.edu.cn

Abstract

Precise incorporation of metal single-atom (SA) active sites into covalent organic frameworks (COFs) offers a powerful approach to enhance electrochemiluminescence (ECL) by facilitating co-reactant activation and charge transport. However, metal coordination usually triggers intramolecular electron-transfer quenching that degrades the ECL efficiency of COFs. Herein, we construct a pyrene-phenanthroline COF with coordinated Ag SA (Ag_{SA}/PP-COF) that breaks the catalysis-quenching dilemma of metals, achieving enhanced ECL performance. Density functional

theory calculations reveal that, among the screened metal catalysts, the d^{10}-configurated Ag (I) center exhibits the weakest electron coupling with the nitrogen atoms of PP-COF's phenanthroline units. This minimal perturbation ensures that the framework's intrinsic luminescence is largely retained. Specifically, Ag_{SA} serves as highly efficient active sites, facilitating co-reactant adsorption and activation while accelerating interfacial electron transfer kinetics. Remarkably, the resultant Ag_{SA}/PP-COF exhibits a 4.5-fold enhancement in ECL intensity. Moreover, Ag_{SA}/PP-COF enables the construction of a highly sensitive ECL enzymatic biosensor for organophosphorus pesticide detection. This work provides a universal strategy for the design of high-performance solid-state ECL emitters.

Introduction

Solid-state electrochemiluminescence (ECL) is a light-emitting phenomenon driven by electrochemical reactions, where emitters typically confined at the electrode surface undergo redox processes to generate excited states that decay radiatively[1-4]. Donor-acceptor (D-A) conjugated covalent organic frameworks (COFs), with the features of long-range order, flexible structure regulation, and atomically precise, offer a compelling design strategy for solid-state ECL emitters by facilitating intramolecular charge transfer[5-8]. However, the absence of redox-active metal centers compromises the catalytic cycle for generating reaction intermediates and impedes efficient electron pathways for charge injection, thereby restricting co-reactant activation and resulting in a low ECL efficiency[9, 10].

Integrating catalytically active metal sites with luminophores into a single COF structural unit presents an effective solution to the aforementioned challenges. It shortens the reaction pathway between emitters and co-reactants, thereby accelerating electron transport and mitigating energy loss during electrochemical processes[11-13]. Single-atom catalysts (SACs) exhibit maximized metal utilization efficiency, with the well-defined metal centers serving as highly active catalytic sites that can effectively promote the activation of co-reactants in the ECL processes[14-17]. However, the integration of single-atom active sites into COFs for ECL remains largely unexplored, primarily due to challenges of ECL quenching arising from electron transfer between luminescent linkers and metal sites[18-20]. Specifically, coordination between metal atoms and COF induces orbital overlap, facilitating electron transfer from donor units to acceptors or directly to metal centers. This redistribution of electrons alters the intrinsic donor-acceptor character of the COFs,

perturbing their ground-state electronic structure. As a result, the formation and relaxation of excited states are disrupted, leading to ECL quenching. Therefore, a thorough investigation of the structure-activity relationship between metal single-atom sites and COFs to balance catalytic efficiency and quenching effects for boosting ECL performance still poses a significant challenge.

Herein, guided by density functional theory (DFT) calculations, a series of metal single atoms has been screened to enhance interfacial electron transfer efficiency and catalytic activity within the pyrene-phenanthroline COF (PP-COF). Our findings reveal that the Ag atom with a d^{10} electronic configuration induces minimal perturbation to the charge distribution of nitrogen atoms in the phenanthroline units of PP-COF after coordination, which is anticipated to impart only slight ECL quenching to the PP-COF (**Fig. 1**). Both experimental and theoretical studies demonstrate that Ag_{SA}/PP-COF narrows the band gap, promoting electron transfer and accelerating PP-COF excited-state formation. Moreover, peroxydisulfate can be efficiently adsorbed and activated, generating abundant radical intermediates. Compared with pristine PP-COF, Ag_{SA}/PP-COF exhibits a remarkable 4.5-fold enhancement in ECL, along with a positive shift of the corresponding potential from -1.5 V to -1.2 V. Note that the universality of this strategy was validated by extending it to two other COFs commonly used for metal coordination (2,2'-bipyridine and porphyrin-based frameworks). Finally, the resultant Ag_{SA}/PP-COF-based sensor was developed for sensitive detection of organophosphorus pesticides.

Results

1,3,6,8-tetrakis(4-aminophenyl)pyrene (PyTBA) and 4,4’-(1,10-phenanthroline-3,8-diyl)dibenzaldehyde (PDDB) are used as building blocks to synthesize a model D-A PP-COF via

a solvothermal method for conceptual validation[21]. The ordered porous structure in PP-COF, along with the abundant N atoms in the phenanthroline units, creates an ideal environment for the precise coordination of metal single atoms, thereby ensuring the uniform dispersion of active sites (**Fig. 2a**). Understanding the extent of electronic coupling between metals and COFs is critical for balancing catalytic activation and excited-state quenching. Frontier molecular orbital theory offers a fundamental approach for depicting metal-support orbital interactions[22-23]. DFT calculations reveal that the lowest unoccupied molecular orbital (LUMO) level of PP-COF (-2.43 eV) lies significantly higher than those of certain metal atoms (Fe: -2.87 eV; Co: -2.76 eV; Ni: -2.67 eV; Pt: -2.98 eV). This strong electronic coupling drives unfavorable electron transfer during ECL generation, wherein injected electrons preferentially migrate from PP-COF to metal centers rather than participating in the formation of excited states[24]. In contrast, the d^{10} group metal atoms (Cu: -0.68 eV; Ag: -0.71 eV; Au: -0.74 eV) exhibit higher LUMO energies than PP-COF, producing an energy barrier that leads to weak electronic coupling and preserves the ECL-active excited-state (**Fig. 2b**). To unravel the influence of different metals on the electron distribution in the framework after coordination with PP-COF, DFT simulations on characteristic fragments of M/PP-COFs were performed. Within the PP-COF architecture, the highest occupied molecular orbital (HOMO) is predominantly localized on the pyrenyl areas. The observed electronic localization can be attributed to the intrinsic electron-donating propensity of the pyrene units, which consequently suggests a preferential formation of cationic radical species at these specific sites[25-26]. LUMO is distributed on the phenanthroline parts (**Fig. 2c**). As shown in **Supplementary Fig. 1**, when metal atoms (Fe, Co, Ni, Pt) coordinate with phenanthroline in PP-COF, the HOMO is primarily resided

the metal and the phenanthroline moieties, indicating the occurrence of intramolecular charge transfer[27]. In contrast, for d^{10} group metals (Cu, Ag, Au), the HOMO distribution of PP-COF remains largely unaffected. Furthermore, the LUMO energy level of Ag_{SA}/PP-COF decreases to -2.55 eV compared to pristine PP-COF (-2.43 eV), facilitating more electron transfer from the HOMO, thereby promoting the generation of excited states and ultimately improving the ECL efficiency[28-29]. Theoretical calculations reveal that the charge variation on the N atoms in phenanthroline before and after coordination with Ag is minimal, suggesting that Ag doping is expected to exert the least impact on the intrinsic ECL signal of PP-COF (**Fig. 2d and Supplementary Fig. 2**). Notably, Ag exhibits a higher d-band center closer to the Fermi level compared to Au, which strengthens the adsorption of reaction intermediates and consequently facilitates subsequent electrochemical processes (**Fig. 2e**)[30]. Taking advantage of minimal interference with the framework's intrinsic ECL properties and exceptional co-reactant activation capability, Ag as the optimal catalytic center for PP-COF-based ECL systems is greatly expected.

In the Fourier transform infrared spectroscopy (FT-IR) spectrum of PP-COF, the significant weakening of the characteristic peaks for the aldehyde group (around 1693 cm^{-1}) and amine group (3342 cm^{-1}), along with the appearance of a prominent C=N vibration peak at 1619 cm^{-1}, revealing the formation of the imine linkage (**Fig. 3a**). The ^{13}C solid-state nuclear magnetic resonance (NMR) spectra further confirm the presence of the imine carbons at 149.9 ppm for PP-COF[31]. Additionally, the peaks located at 143.6 ppm and 139.9 ppm belonged to the alpha position of the o-phenanthroline nitrogen atom to the tertiary carbon and quaternary carbon, respectively (**Fig. 3b**). The crystalline structure of PP-COF is confirmed by powder X-ray diffraction (PXRD), with

strong peaks appearing at 2.5, 3.5, 4.9, 7.5, and 9.9° corresponding to the (100), (110), (200), (300), and (400) lattice planes, respectively (**Supplementary Fig. 3**). The lattice parameters of PP-COF in *P*1 space group are obtained through Pawley refinement against of PXRD pattern (a = 36.49 Å, b = 36.14 Å, c = 3.64 Å, α = β = γ = 90°) (**Supplementary Fig. 4**). Importantly, the PXRD results are similar to the simulated AA-eclipsed stacking mode (unweighted profile R factor (Rp = 5.26%) and weighted-profile R factor (Rwp = 7.42%)). The high crystallinity and AA-stacked arrangement endow the framework with a regular structure, which facilitates efficient intramolecular charge transfer and consequently enhances the ECL performance[32]. The crystallinity of PP-COF remains intact after 12 h exposure to various organic solvents, underscoring its excellent chemical stability (**Supplementary Fig. 5**). Furthermore, the crystal structure of PP-COF is well retained after loading Ag species (**Fig. 3c**). No peak assigned to Ag metal or metal oxide is observed from the PXRD result, indicating that Ag exists in the form of single atoms[33]. Scanning electron microscopy (SEM) images show that PP-COF retains its original morphology after Ag incorporation (**Supplementary Fig. 6**). Transmission electron microscopy (TEM) images demonstrate the well-defined stacked lamellar architecture of PP-COF. High-resolution TEM (HRTEM) image confirms a lattice spacing of 2.2 nm, corresponding to the (010) plane (**Fig. 3d**). Notably, no detectable Ag nanoparticles are observed in the HRTEM image of Ag_{SA}/PP-COF. High-angle annular dark-field scanning TEM (HAADF-STEM) and corresponding energy-dispersive spectroscopy (EDS) mapping images further verify the homogeneous distribution of C, N, and Ag elements within the Ag_{SA}/PP-COF structure (**Fig. 3e**). The atomic-scale distribution of Ag species was further investigated through aberration-corrected HAADF-STEM (AC-HAADF-STEM), which

demonstrates the uniform dispersion of isolated Ag atoms, as evidenced by the presence of bright spots throughout the PP-COF matrix (**Fig. 3f**). The Ag content was determined to be 1.68 wt% by inductively coupled plasma mass spectrometer[34]. The electronic properties and local coordination environment of Ag_{SA} in Ag_{SA}/PP-COF were further elucidated by X-ray photoelectron spectroscopy (XPS). The binding energies of the Ag $3d_{3/2}$ and Ag $3d_{5/2}$ peaks are located at 374.16 eV and 368.08 eV, respectively, which suggests a valence state of Ag between 0 and +1 (**Fig. 3g**). In contrast to PP-COF, the high-resolution N 1*s* spectrum of Ag_{SA}/PP-COF exhibits an additional peak at 399.76 eV, which is attributed to the N atoms of the phenanthroline units coordinating with Ag (**Fig. 3h**)[35-36]. The nitrogen adsorption/desorption isotherm of PP-COF was analyzed at 77 K to assess the porosity and surface area. The type IV adsorption isotherm indicated the presence of typical mesopores in the structure. The Brunauer-Emmett-Teller (BET) surface area of PP-COF was calculated to be 1231 $m^2 g^{-1}$, with an average pore diameter of 3.94 nm. The incorporation of Ag decreases the BET surface area of Ag_{SA}/PP-COF to 731 $m^2 g^{-1}$, which can be attributed to the partial occupation of pores by the anchored Ag_{SA} (**Fig. 3i**). However, the single atom loading is not sufficient to significantly alter the pore size, as the pore diameter is primarily determined by the framework structure of the COFs (**Supplementary Fig. 7**). Thermogravimetric analysis (TGA) demonstrates that the Ag_{SA}/PP-COF maintains excellent thermal stability, exhibiting significant weight loss observed only above ~400 °C under a nitrogen atmosphere, with decomposition behavior comparable to the pristine PP-COF (**Supplementary Fig. 8**). Ultraviolet-visible (UV-vis) absorption spectroscopy reveals a distinct red shift in the absorption edge of Ag_{SA}/PP-COF in comparison to PP-COF, indicating enhanced visible-light harvesting capability (**Supplementary**

Fig. 9a). This phenomenon originates from the vibrational broadening of PP-COF and enhanced delocalization induced by Ag_{SA} chelation[37-38]. Furthermore, Tauc plot analysis demonstrates that the band gaps of PP-COF and Ag_{SA}/PP-COF are 1.81 eV and 1.66 eV, respectively (**Supplementary Fig. 9b**). The incorporation of Ag_{SA} enhances the donor-acceptor interactions and effectively reduces the bandgap, thereby facilitating the electronic transition from the ground state to the excited state. Mott-Schottky analysis provides further insight into the electronic band structure, revealing a negative shift of the conduction band potential from -0.79 V in pristine PP-COF to -0.99 V in Ag_{SA}/PP-COF. This shift indicates an enhanced reductive capability of the modified material (**Supplementary Fig. 10**)[39]. Steady-state photoluminescence (PL) spectroscopy reveals that the PL intensity of Ag_{SA}/PP-COF exhibits a slight quenching compared to that of pristine PP-COF, accompanied by a minor blue shift in the emission peak (**Supplementary Fig. 11a**). This phenomenon can be attributed to the expansion of interlayer spacing in PP-COF induced by Ag_{SA} incorporation, which reduces the interlayer π-π stacking interactions[40]. The photoluminescence quantum yield (PLQY) exhibits only a marginal decrease from 1.64% for PP-COF to 1.49% for Ag_{SA}/PP-COF, demonstrating that the Ag_{SA} incorporation largely preserves the intrinsic luminescent properties of the PP-COF. In contrast, other M/PP-COFs (M = Au, Cu, Pt, Fe, Co, Ni) all exhibit more pronounced and varying degrees of PLQY reduction, reflecting significant luminescence quenching (**Supplementary Fig. 11b**). XPS analysis reveals that Ag doping leads to the smallest shift in the binding energy of the pyridinic N 1*s* peak (**Supplementary Fig. 12**). This observation suggests that the Ag-N interaction results in either the weakest initial-state charge transfer or the strongest final-state shielding effect among the metals studied. The

time-resolved photoluminescence (TR-PL) reveals that the fluorescence lifetime increases from 2.34 ns for PP-COF to 2.70 ns for Ag_{SA}/PP-COF, demonstrating that the Ag_{SA} doping slightly extends the carrier lifetimes (**Supplementary Fig. 13**).

The electrochemical behavior of the PP-COF and Ag_{SA}/PP-COF was examined during reduction and oxidation processes. The cyclic voltammetry (CV) curve of PP-COF exhibits an anodic peak at +1.4 V, corresponding to the oxidation of pyrene units, and a cathodic peak at -1.41 V, attributed to the reduction of pyrene units[25,26]. After the introduction of Ag_{SA}, both anodic and cathodic currents significantly increase, while the redox peaks of pyrene remain preserved (**Supplementary Fig. 14**). Subsequently, we systematically evaluated the co-reactant-based ECL performance using several common small-molecule co-reactants. Among the tested co-reactants (H_2O_2, N_2H_4•H_2O, $C_2O_4^{2-}$, and $K_2S_2O_8$), $K_2S_2O_8$ demonstrates exceptional efficacy in amplifying the ECL emission of PP-COF (**Supplementary Fig. 15**). As shown in **Fig. 4a**, CV curves reveal that Ag_{SA}/PP-COF exhibits a significantly enhanced reduction current compared to pristine PP-COF, indicating superior electrocatalytic activity[41]. Notably, the electrochemical reduction peak of $K_2S_2O_8$ in the Ag_{SA}/PP-COF system shifts positively from -1.0 V to -0.69 V (vs. Ag/AgCl), suggesting that the Ag_{SA} sites efficiently catalyze the reduction of $K_2S_2O_8$. Consequently, the ECL emission of Ag_{SA}/PP-COF commences at -1.2 V, whereas PP-COF exhibits negligible luminescence until -1.5 V. Remarkably, the maximum ECL intensity of Ag_{SA}/PP-COF at -1.8 V surpasses that of PP-COF by a factor of 4.5, which corresponds to an approximately 4.1-fold greater ECL enhancement compared to the system containing an equivalent amount of free Ag^+ in the electrolyte (**Supplementary Fig. 16**). This phenomenon demonstrates that Ag_{SA} doping effectively decreases

the activation energy of the ECL reaction process in PP-COF, thereby significantly enhancing the ECL signal. In contrast, although the other M/PP-COFs (M = Cu, Au, Pt, Fe, Co, Ni) composites exhibit enhanced reduction currents (**Supplementary Fig. 17**), they all show varying degrees of ECL quenching, which is consistent with theoretical predictions (**Fig. 4b and Supplementary Fig. 18**). The role of dissolved O_2 in the ECL process was investigated by conducting experiments under O_2, air, and N_2-saturated electrolyte conditions. The ECL signal in the O_2-saturated solution surpasses even that in the air-saturated $K_2S_2O_8$ solution, while N_2 saturation leads to a moderate decline in intensity due to diminished reactive oxygen species generation (**Supplementary Fig. 19**). These findings corroborate that O_2 may function as a secondary co-reactant, further oxidizing intermediates or prolonging radical pathways, thereby amplifying ECL. Notably, despite the limited contribution of dissolved O_2 to the overall ECL mechanism, we intentionally preserve ambient O_2 levels during measurements to mirror real-world biological environments. To elucidate the influence of metal sites on the ECL performance, S^{2-} is employed to selectively shield Ag_{SA} active sites. Remarkably, the ECL efficiency of the system is significantly suppressed due to the strong coordination between Ag_{SA} sites and S^{2-} anions (**Fig. 4c**), providing compelling evidence for the pivotal role of Ag_{SA} in the ECL process[42]. Tafel analysis serves as a powerful tool for evaluating electrochemical reaction kinetics, where a smaller Tafel slope indicates faster electrode kinetics and a more pronounced current increase. The Tafel slopes for PP-COF and Ag_{SA}/PP-COF were calculated to be 809.2 and 293.1 mV dec^{-1}, respectively, demonstrating that the Ag_{SA}, as a co-reaction accelerator, effectively enhances the reaction kinetics (**Fig. 4d**). Electrochemical impedance spectroscopy (EIS) analysis reveals a significantly smaller semicircle radius for

Ag_{SA}/PP-COF compared to PP-COF, indicating a lower charge transfer resistance (**Supplementary Fig. 20**). Moreover, *operando* EIS provides further insights into the kinetic distinctions between the PP-COF and M/PP-COFs during the electrochemical process. Specifically, in the Ag_{SA}/PP-COF system, as the potential sweeps negatively from -0.2 V to -0.6 V, a continuous decrease in the high-frequency phase angle is observed, which is attributed to the reduction of $K_2S_2O_8$. Upon further polarization to the potential range of -0.7 V to -1.0 V, a low-frequency phase angle emerges and progressively increases, indicative of the accumulation of radical intermediates at the electrode-catalyst interface, manifesting as an enhancement in the interfacial chemical pseudocapacitance[43]. When the potential exceeds -1.1 V, the low-frequency phase angle disappears, suggesting the rapid consumption of the accumulated radical intermediates. Simultaneously, the high-frequency phase angle continues to decrease with increasing negative potential, indicating accelerated interfacial charge transfer and the system entering a high-efficiency luminescence steady state characterized by rapid electron transfer (**Fig. 4e**). This behavior corresponds to the intrinsic reduction of the COF occurring at the high-frequency interface in PBS (**Supplementary Fig. 21**). Similar stage evolution is also observed in other M/PP-COFs systems. All M/PP-COFs exhibit smaller phase angles in the high-frequency region compared to the PP-COF, indicating that the introduction of metal sites generally enhances the electrochemical reduction capability of the materials, favoring the generation of the active species $COF^{\bullet-}$. However, different M/PP-COFs exhibit distinct electron transfer kinetics (**Supplementary Fig. 22**). In addition, compared to PP-COF (RSD = 2.39%), the ECL emission of Ag_{SA}/PP-COF exhibited significantly enhanced stability (RSD = 1.74%) (**Fig. 4f**). This improvement in stability is closely associated with the

mitigation of electrode passivation caused by the excessive injection of high-energy electrons. The incorporation of Ag_{SA} effectively regulates the electron transfer process at the electrode-electrolyte interface, thereby reducing the accumulation of high-energy states that lead to electrode degradation. We further investigated the structural stability of the Ag_{SA}/PP-COF after 20 consecutive ECL signal cycles. Post-cycling characterizations by SEM and TEM reveal that the Ag_{SA}/PP-COF structure retained its original morphology without observable degradation or collapse (**Supplementary Figs. 23a,b**). Elemental mapping images further reveal a homogeneous distribution of C, N, and Ag after cycling, with no evidence of Ag aggregation or nanoparticle formation, confirming that the Ag_{SA} sites remained intact and anchored within the framework after testing (**Supplementary Fig. 23c**). This remarkable stability can be attributed to the coordination interaction between the metal centers and the functional groups within the COF skeleton, combined with the spatial confinement effect of the porous framework, which collectively stabilizes the catalytically active sites[38].

The co-reactant $K_2S_2O_8$ readily undergoes electrochemical reduction, generating highly oxidizing intermediates (hydroxyl radicals (•OH) and sulfate radicals ($SO_4^{\bullet-}$)) in PBS solution. To unravel the identity of reactive intermediates governing the $K_2S_2O_8$ activation pathway, we employ isopropanol (IPA) and tert-butyl alcohol (TBA) as scavengers for •OH and $SO_4^{\bullet-}$. Strikingly, the introduction of IPA induces 82% suppression of the ECL signal, whereas TBA causes less than 50% attenuation (**Fig. 5a**). The divergent scavenging efficiencies align with the distinct reaction kinetics of IPA ($k = 1.9 \times 10^9\ M^{-1}\ s^{-1}$ for •OH; $k = 7.4 \times 10^8\ M^{-1}\ s^{-1}$ for $SO_4^{\bullet-}$) and TBA ($k = 3.8 \times 10^8\ M^{-1}\ s^{-1}$ for •OH; $k = 4.0 \times 10^5\ M^{-1}\ s^{-1}$ for $SO_4^{\bullet-}$), demonstrating that •OH and $SO_4^{\bullet-}$ serve as the primary

co-reactive intermediates in this ECL system[44-45]. The enhanced ECL is predominantly driven by $SO_4^{\bullet-}$, which is primarily generated through homolytic cleavage of $K_2S_2O_8$ during the electrochemical reduction process. Subsequent hydrolysis of $SO_4^{\bullet-}$ in aqueous media facilitates its partial conversion to •OH through the proton-coupled electron transfer reaction ($SO_4^{\bullet-} + H_2O \rightarrow$ $\bullet OH + SO_4^{2-} + H^+$) to synergistically enhance the excitation of PP-COF luminophores[46-47]. Spin-trapping electron paramagnetic resonance (EPR) analysis employing 5,5-dimethyl-1-pyrroline N-oxide (DMPO) under a constant potential of -1.8 V unambiguously identified two radical species, exhibiting distinct hyperfine splitting patterns for [DMPO-SO_4]• and [DMPO-OH]•[48]. Furthermore, Ag_{SA}/PP-COF demonstrates significantly enhanced [DMPO-SO_4]• and [DMPO-OH]• signal intensities compared to PP-COF, evidencing the superior capability of Ag_{SA} to facilitate $K_2S_2O_8$ adsorption and activation (**Fig. 5b**). The electrochemical adsorption behaviors of PP-COF and Ag_{SA}/PP-COF were further investigated through double potential step chronocoulometry. The calculated Faraday adsorption charges (Q_{ads}) for $K_2S_2O_8$ were determined to be 3.57 and 6.92 μC for PP-COF and Ag_{SA}/PP-COF, respectively, demonstrating significantly enhanced adsorption capability of $K_2S_2O_8$ on Ag_{SA}/PP-COF (**Fig. 5c and Supplementary Fig. 24**). Upon adsorption of $K_2S_2O_8$ onto the Ag_{SA}/PP-COF surface, the Ag 3*d* XPS peak shifts toward lower binding energy, indicating electron transfer from $K_2S_2O_8$ to the Ag sites. This shift highlights an increase in electron density at the Ag active centers during adsorption (**Supplementary Fig. 25**). These Ag centers, serving as Lewis acid sites, strengthen the interaction with $K_2S_2O_8$ and thereby facilitate its electrocatalytic reduction, which is crucial for enhancing the overall ECL performance[49]. *In situ* FTIR spectroscopy was employed to investigate the reaction pathway of

$K_2S_2O_8$ activation. In the potential range of -0.1 to -0.4 V, the increase in peak intensity at 1236 cm^{-1} corresponds mainly to the enhanced vibrational feature of the S-O bond, which is associated with increased adsorption of $K_2S_2O_8$. Upon applying a negative potential exceeding -0.5 V, an increase in the characteristic peak of SO_4^{2-} groups (~1008 cm^{-1}) was observed, accompanied by a continuous consumption of the O-O group peak (~1228 cm^{-1}), attributed to the cleavage of the O-O bond in $K_2S_2O_8$ (**Fig. 5d**). The prominent absorption band at ~3256 cm^{-1} is associated with adsorbed •OH species, resulting from the reaction between $SO_4^{\bullet-}$ and solution-phase -OH groups that enhances •OH adsorption (**Fig. 5e**). For Ag_{SA}/PP-COF, the higher peak intensity indicates its superior capability to facilitate the homolytic cleavage of the O-O bond in $K_2S_2O_8$, resulting in significantly increased radical generation. DFT calculations were performed to elucidate the reduction pathways of $K_2S_2O_8$, with model structures constructed for its adsorption on either the phenanthroline unit or the Ag_{SA} site. The Gibbs free energy profiles reveal that the rate-determining step involves $S_2O_8^{2-}$ binding to the adsorption site, where Ag_{SA}/PP-COF exhibits a significantly lower energy change (0.57 eV) compared to pristine PP-COF (1.05 eV). This enhanced adsorption capability of Ag_{SA}/PP-COF facilitates subsequent reaction steps, demonstrating its superior catalytic activity (**Fig. 5f**). Overall, a mechanistic understanding of the enhanced ECL observed in Ag_{SA}/PP-COF is provided. During the electrochemical process, Ag_{SA}/PP-COF undergoes initial reduction via electron injection into its LUMO, leading to the formation of anionic radical species (Ag_{SA}/PP-COF$^{\bullet-}$). Concurrently, the co-reactant $K_2S_2O_8$ is oxidized to produce $SO_4^{\bullet-}$, which subsequently oxidizes the Ag_{SA}/PP-COF framework to generate cationic radicals (Ag_{SA}/PP-COF$^{\bullet+}$). The annihilation of Ag_{SA}/PP-COF$^{\bullet-}$ and Ag_{SA}/PP-COF$^{\bullet+}$ via efficient intra-reticular charge

transfer then releases energy, giving rise to ECL emission[25]. Importantly, the Ag_{SA} sites act as an efficient catalyst that promotes the generation of $SO_4^{\bullet-}$, thereby significantly enhancing the overall ECL intensity (**Supplementary Eqs. 1-5**).

To systematically elucidate the atomic-level modulation of ECL properties in COFs, we design two structurally distinct COF systems based on 2,2'-bipyridine and porphyrin building blocks. (**Supplementary Fig. 26**). Remarkably, both Ag_{SA}-loaded COF composites exhibit significantly enhanced ECL intensities compared to their pristine COFs (**Supplementary Fig. 27**). This universal enhancement effect, observed across distinct COF architectures, demonstrates the broad applicability of Ag_{SA} in amplifying the ECL signals of COFs, thereby establishing a versatile strategy for improving the luminescence efficiency of this emerging class of materials.

Organophosphorus pesticides (OPs) are extensively utilized in agricultural production, but their excessive misuse and environmental persistence have raised significant public health concerns. The over-inhibition of acetylcholinesterase (AChE) activity by OPs can lead to severe neurological damage and various adverse health effects. Therefore, the development of a highly sensitive biosensing platform for OP detection is of paramount importance[50-51]. We present a proof-of-concept ECL system for OP detection using an Ag_{SA}/PP-COF as the ECL emitter. The detection mechanism relies on the enzymatic hydrolysis of acetylthiocholine chloride (ATCl) by AChE to generate thiocholine (TCh) in situ. The sulfhydryl group of TCh, serving as the reactive center, is oxidized by $K_2S_2O_8$, producing the corresponding disulfide species (dithiobischoline) and SO_4^{2-}. As the co-reactant $K_2S_2O_8$ near the electrode surface is consumed, the concentration of $S_2O_8^{2-}$ participating in the ECL reaction decreases, resulting in a diminished ECL signal (**Fig. 6a**). In the

absence of AChE, ATCl remains stable and does not undergo significant spontaneous reaction with $K_2S_2O_8$. Moreover, ATCl is resistant to non-enzymatic hydrolysis, thus preventing the generation of reducing TCh (**Supplementary Fig. 28**). As a result, the concentration of $K_2S_2O_8$ in solution remains largely unchanged, sustaining a consistently high ECL signal. Upon incubation with OPs, the inhibition of AChE activity leads to the recovery of the ECL signal. Notably, the cathodic ECL intensity increases progressively with higher OP concentrations (**Fig. 6b**). A linear relationship between the logarithm of OPs concentration (0.1-1000 ng mL^{-1}) and ECL intensity was established, with a regression equation of $y = 1348.4 \lg C_{OPs} + 5691$ ($R^2 = 0.991$) (**Fig. 6c**). The limit of detection is determined to be 0.048 ng mL^{-1}, superior to those of PP-COF and previous works **(Supplementary Fig. 29 and Table 1)**. To evaluate selectivity, potential interferents (including common ions, urea, dopamine, and glucose at ten-fold higher concentrations) are tested under identical conditions. No significant ECL signal variations are observed, confirming the biosensor's outstanding specificity for OPs (**Fig. 6d**). Moreover, the ECL sensing platform exhibits excellent stability, as evidenced by the low RSD of 2.7% and 2.1% (**Fig. 6e**). The reproducibility of the sensor is further evaluated by fabricating five electrodes under identical conditions and measuring their ECL responses toward OPs at the same concentration (0.1 ng mL^{-1}). The RSD was calculated to be 1.11%, indicating excellent reproducibility (**Fig. 6f**). In addition, the ECL platform successfully detected OPs in spiked tap water samples with excellent recovery rates (93.58-102.4%), demonstrating its practical applicability for environmental monitoring (**Supplementary Table 2**).

Discussion

In conclusion, DFT calculations were employed to screen the degree of electronic coupling between PP-COF and various catalytically active metals as a key descriptor, revealing Ag-functionalized PP-COF as the most promising candidate for enhancing ECL performance. Experimental results demonstrated that Ag_{SA}/PP-COF exhibits significantly enhanced ECL intensity and a lower reduction potential compared to pristine PP-COF, whereas other M/PP-COF composites showed varying degrees of quenching, consistent with theoretical predictions. This enhancement arises from the judicious incorporation of Ag_{SA}, which minimally perturbs the intrinsic luminescence of PP-COF while simultaneously accelerating the interfacial electron transfer and catalytically cleaving the O-O bond in $K_2S_2O_8$ to generate increased concentrations of reactive radical species. This work presents a generalizable strategy for amplifying the ECL performance of COF-based emitters and provides critical insights into the design of advanced co-reactant accelerators for COF-ECL systems.

Methods

Chemicals and reagents

1,3,6,8-tetrakis(4-aminophenyl)pyrene (PyTBA), 4,4'-(1,10-phenanthroline-3,8-diyl)dibenzaldehyde (PDDB), and $PtCl_2$ were obtained from Bide Pharmatech Co., Ltd. (Shanghai, China). Tetrahydrofuran (THF), methanol, potassium dihydrogen phosphate (KH_2PO_4), dipotassium hydrogen phosphate (K_2HPO_4), $FeCl_3$, $CoCl_2 \cdot 6H_2O$, and $NiCl_2 \cdot 6H_2O$ were purchased from Sinopharm Chemical Reagent Co., Ltd (Shanghai, China). Silver acetate was acquired from Energy Chemical (Saen Chemical Technology (Shanghai) Co., Ltd.). Acetylthiocholine (ATCh), 5,5-dimethyl-1-pyrroline 1-oxide (DMPO), dopamine (DA), glucose (Glu), potassium

peroxodisulfate ($K_2S_2O_8$), mesitylene, n-butylalcohol, acetic acid, $Cu(COOCH_3)_2$, were supplied from Aladdin Chemical Reagent Co., Ltd (Shanghai, China). Nafion and acetylcholinesterase (AChE), $KAuCl_4$, and urea were bought from Macklin Biochemical Co., Ltd. (Shanghai, China). Glyphosate was purchased from North Weiye Metrology Technology Research (Beijing, China). All the chemicals mentioned above were analytical reagents. The deionized water (18.2 MΩ·cm) was produced using a Milli-Q water purification apparatus (Millipore, MA, USA).

Instruments and characterizations

Fourier transform infrared spectroscopy (FT-IR) spectra were recorded on a TENSOR27 (Germany). Solid-state ^{13}C nuclear magnetic resonance (NMR) spectra were acquired using a Bruker AVANCE III 600 M (Bruker, Germany). Powder X-ray diffraction (PXRD) measurements were performed by a D8 ADVANCE (Bruker, Germany). Transmission electron microscopy (TEM) was performed on a Talos F200X G2 (Thermo Scientific). The aberration-corrected high-angle annular dark-field scanning transmission electron microscopy (AC-HAADF-STEM) was conducted using a JEM-ARM300F (JEOL, Japan). Scanning electron microscopy (SEM) images were obtained from the Gemini SEM 300 (ZEISS). Nitrogen adsorption/desorption isotherms were measured on a fully automatic physical adsorption analyzer (BELSORP MAX G). X-ray photoelectron spectroscopy (XPS) was performed on an ESCALAB QXi. The element contents were determined by an inductively coupled plasma mass spectrometer (ICAP RQ). Electron paramagnetic resonance (EPR) measurements were carried out on an EMXmicro-6/1 (Bruker, Germany). Thermogravimetric analysis (TGA) was conducted by using a simultaneous thermal analyzer (Mettler-Toledo, Switzerland). Ultraviolet-visible (UV-Vis) diffuse-reflectance

absorption spectra were recorded on a Cary 100 UV-Vis spectrophotometer (Agilent Technologies). Photoluminescence (PL) spectra and time-resolved fluorescence emission spectra were measured at room temperature on an FLS1000 fluorescence spectrophotometer (Edinburgh Instruments). *In situ* Attenuated-total-reflection Fourier transform infrared spectroscopy (ATR-FTIR) spectroscopy was performed on a Nicolet iS50 FTIR spectrometer (Thermo). ECL signals were recorded on the IFFM-E capillary electrophoresis ECL analytical system (Xi'an Remax Electronics Science & Technology Co. Ltd.).

Synthesis of PP-COF

Initially, 1,3,6,8-tetrakis(4-aminophenyl)pyrene (PyTBA, 0.025 mmol) and 4,4'-(1,10-phenanthroline-3,8-diyl)dibenzaldehyde (PDDB, 0.05 mmol) were dissolved in a mixture of mesitylene and n-butanol (0.1 mL/0.9 mL) in a 10 mL Pyrex tube. The solution was sonicated for 5 min, followed by the addition of 6 M acetic acid (0.1 mL) as a catalyst. The mixture was then degassed by three freeze-pump-thaw cycles and sealed under vacuum. Solvothermal reaction was carried out at 120 °C for 72 h. The resulting orange solid was collected by filtration, washed sequentially with THF and methanol to eliminate residual unreacted monomers, and finally dried under vacuum at 80 °C overnight.

Synthesis of M/PP-COFs

Briefly, PP-COF (20 mg) was uniformly dispersed in methanol (MeOH, 16 mL). Subsequently, a solution of silver acetate (4 mL, 10 mM) was added, and the resulting suspension was stirred at room temperature for 6 h (500 rpm) to ensure complete metal incorporation. The product was collected by filtration, washed thoroughly with methanol and deionized water to remove unreacted

precursors, and dried under vacuum at 60 °C to afford Ag_{SA}/PP-COF. Other M/PP-COF analogs were prepared following the same protocol, except that the silver acetate was replaced by the corresponding metal precursor, including $FeCl_3$, $CoCl_2•6H_2O$, $NiCl_2•6H_2O$, $PtCl_2$, $Cu(COOCH_3)_2$, or $KAuCl_4$.

Electrochemical and ECL tests

The electrochemical experiments were conducted using a standard three-electrode system, comprising an Ag/AgCl reference electrode, a Pt sheet counter electrode, and a glassy carbon electrode (GCE, 3 mm diameter) modified with M/PP-COF as a working electrode. All M/PP-COF-modified electrodes were prepared as follows: the synthesized M/PP-COF was dispersed in a water/ethanol mixture (7:3, v/v), followed by the addition of 10 μL of a 5 wt% Nafion solution. The mixture was sonicated to yield a homogeneous dispersion with a concentration of 2 mg mL^{-1}. Subsequently, 10 μL of the resulting M/PP-COF suspension was drop-cast on the GCE surface and dried at 50 °C. ECL measurements were conducted in 3 mL of PBS buffer solution (0.1 M, pH 7.4) containing 0.1 M $K_2S_2O_8$. The ECL signals were recorded during cyclic voltammetry scans from 0 to -1.8 V at a scan rate of 0.1 V s^{-1}, with the photomultiplier tube biased at 700 V.

EPR experiments

The generation of free radicals was verified by spin trapping with DMPO, followed by EPR analysis. The electrolyte was sampled during electrolysis at a fixed applied potential of -1.8 V. Subsequently, DMPO (30 μL) was introduced, and the resulting EPR spectra were recorded.

EIS and *in-situ* EIS measurements system

EIS measurements were carried out over a frequency range of 0.1 Hz to 100000 Hz with a signal

amplitude of 5 mV using a CHI-660 electrochemical workstation in 5 mM $[Fe(CN)_6]^{3-/4-}$ containing 1 M KCl as the supporting electrolyte. *Operando* EIS measurements were carried out over a frequency range of 1 Hz to 100000 Hz with a signal amplitude of 5 mV using a CHI-660 electrochemical workstation in 0.1 M PBS (pH 7.4). The applied potential was stepped from -0.2 V to -1.8 V. Electrochemical responses were recorded both in the absence and presence of 0.1 M $K_2S_2O_8$.

Mott-Schottky measurements

The Mott-Schottky measurements were performed using a standard three-electrode configuration, consisting of a working electrode (indium tin oxide (ITO) slices), a counter electrode (Pt wire), and a reference electrode (Ag/AgCl saturated with KCl(aq)). The measurements were carried out at the open-circuit potential in a 0.5 M Na_2SO_4 electrolyte at a fixed frequency of 1000 Hz. The conduction band position was taken to be approximately equal to the flat-band potential, which was determined by extrapolating the linear region of the Mott-Schottky plot to the x-axis intercept.

Electrochemical *in-situ* FTIR test.

The formation of reaction intermediates during electrochemical reduction was probed by *in-situ* FTIR spectroscopy using a Thermo iS50 spectrometer equipped with a liquid-nitrogen-cooled mercury-cadmium-telluride (MCT) detector. PP-COF and Ag_{SA}/PP-COF modified silicon crystal plated with gold served as the working electrodes, with Ag/AgCl and a Pt sheet as the reference and counter electrodes, respectively. All measurements were conducted in 0.1 M PBS (pH 7.4) containing 0.1 M $K_2S_2O_8$. The applied potential was stepped from -0.1 V to -1.8 V in increments of 0.1 V.

OPs detection

First, AChE was mixed with various concentrations of OPs (0.1, 0.5, 1, 10, 100, and 1000 ng mL^{-1}) in a 96-well plate and incubated for 15 min at ambient temperature. Subsequently, 6 μL of this AChE/OPs mixture was incubated with the modified electrode (Ag_{SA}/PP-COF/GCE), and the ECL response was measured in PBS (0.1 M, pH 7.4) containing 0.5 mM ATCl and 0.1 M $K_2S_2O_8$. For selectivity evaluation, the same protocol was followed, except that OPs (100 ng mL^{-1}) were replaced by potential interfering species (1 μg mL^{-1}), including Na^+, Ca^{2+}, SO_4^{2-}, Cl^-, glucose (Glu), dopamine (DA), and urea.

Assay of the OPs in tap water

Standard samples of varying concentrations were prepared using the standard addition method. The detection procedure for real samples was analogous to that described above.

Theoretical calculations

Density functional theory (DFT) calculations on the molecular building units were performed using the Vienna Ab Initio Simulation Package (VASP). The exchange-correlation functional was treated with the generalized gradient approximation (GGA) in the Perdew-Burke-Ernzerhof (PBE) form, and the projector augmented wave (PAW) method was employed to describe electron-ion interactions. Long-range van der Waals interactions were accounted for using the DFT-D3 correction[52]. Integration over the irreducible Brillouin zone was carried out using the Monkhorst-Pack scheme. A plane-wave cutoff energy of 450 eV was adopted. Geometry optimizations were performed with full relaxation of lattice parameters and ionic positions until the total energy converged to within 10^{-5} eV per formula unit and the final forces on all ions were less than 0.02/Å.

Bader charge analysis was conducted using the Bader code on the converged charge density files to evaluate charge transfer behavior. The highest occupied molecular orbital (HOMO) and lowest unoccupied molecular orbital (LUMO) energies, along with their spatial distributions, were extracted from the DFT wavefunctions using the VASPKIT post-processing toolkit[53]. The structural model of PP-COF was constructed using Materials Studio 7.0. Lattice parameters were systematically optimized via iterative Pawley refinement until convergence of the R-weighted pattern (Rwp) and R-pattern (Rp) values, with the refined profiles showing excellent agreement with the experimental data. Full geometry optimizations of atomic positions and total energies were performed using the Forcite module. Gibbs free energy profiles were calculated with the DMol3 code. Electron interactions were described by the PBE exchange-correlation functional within the GGA framework, and van der Waals interactions were treated using Grimme's empirical correction (DFT+D). Self-consistent field (SCF) calculations were conducted with a convergence tolerance of 10^{-6} for both total energy and electronic computations. A Monkhorst-Pack k-point grid of 1 × 1 × 1 was employed for all surface calculations, and a vacuum layer of approximately 20 Å was introduced along the vertical direction to prevent periodic interactions between adjacent slabs.

Data availability

All data are available from the corresponding authors upon request. Source data are provided with this paper.

References

1. Dai L, Fang J, Jiang T, Li Q, Ren X, Li Y, *et al.* Multicomponent supramolecular nanoaggregates with co-emissive electrochemiluminescence. *Matter* 2025, **8:** 102056.

2. Wei X, Zhu M, Cheng Z, Lee M, Yan H, Lu C, *et al.* Aggregation-Induced Electrochemiluminescence of Carboranyl Carbazoles in Aqueous Media. *Angew. Chem. Int. Ed.* 2019, **58:** 3162-3166.

3. Fu W, Qi M, Rong Y, Lin C, Guo W, Su B. Remote On-Paper Electrochemiluminescence-Based High-Safety and Multilevel Information Encryption. *Angew. Chem. Int. Ed.* 2025, **64:** e202420184.

4. Zhu X, Xing H, Xue Y, Li J, Wang E, Dong S. Atom-Anchoring Strategy with Metal–Organic Frameworks for Highly Efficient Solid-State Electrochemiluminescence. *Anal. Chem.* 2021, **93:** 9628-9633.

5. Cao Y, Wu R, Gao Y.-Y, Zhou Y, Zhu J.-J. Advances of Electrochemical and Electrochemiluminescent Sensors Based on Covalent Organic Frameworks. *Nano-Micro Lett.* 2023, **16:** 37.

6. Li Y.-J, Cui W.-R, Jiang Q.-Q, Wu Q, Liang R.-P, Luo Q.-X, *et al.* A general design approach toward covalent organic frameworks for highly efficient electrochemiluminescence. *Nat. Commun.* 2021, **12:** 4735.

7. Luo R, Luo X, Xu H, Wan S, Lv H, Zou B, *et al.* Reticular Ratchets for Directing Electrochemiluminescence. *J. Am. Chem. Soc.* 2024, **146:** 16681-16688.

8. Luo R, Lv H, Liao Q, Wang N, Yang J, Li Y, *et al.* Intrareticular charge transfer regulated electrochemiluminescence of donor–acceptor covalent organic frameworks. *Nat. Commun.* 2021, **12:** 6808.

9. Liu T, Tao Q, Wang Y, Luo R, Ma J, Lei J. Tailored Cis−Trans Isomeric Metal−Covalent Organic Frameworks for Coordination Configuration-Dependent Electrochemiluminescence. *J. Am. Chem. Soc.* 2024, **146:** 18958-18966.

10. Yang Y, Jiang H, Li J, Zhang J, Gao S.-Z, Lu M.-L, *et al.* Highly stable Ru-complex-based metal-covalent organic frameworks as novel type of electrochemiluminescence emitters for ultrasensitive biosensing. *Mater. Horiz.* 2023, **10:** 3005-3013.

11. Fang Y, Yang H, Hou Y, Li W, Shen Y, Liu S, *et al.* Timescale correlation of shallow trap states increases electrochemiluminescence efficiency in carbon nitrides. *Nat. Commun.* 2024, **15:** 3597.

12. Luo R, Zhu D, Ju H, Lei J. Reticular Electrochemiluminescence Nanoemitters: Structural Design and Enhancement Mechanism. *Acc. Chem. Res.* 2023, **56:** 1920-1930.

13. Wu Z, Wen J, Qin Y, Ling L, Jiao L, Zhang R, *et al.* Dual-Site Activation Coupling with a Schottky Junction Boosts the Electrochemiluminescence of Carbon Nitride. *Angew. Chem. Int. Ed.* 2023, **62:** e202308257.

14. Gu W, Wang H, Jiao L, Wu Y, Chen Y, Hu L, *et al.* Single-Atom Iron Boosts Electrochemiluminescence. *Angew. Chem. Int. Ed.* 2020, **59:** 3534-3538.

15. Xia H, Zheng X, Li J, Wang L, Xue Y, Peng C, *et al.* Identifying Luminol Electrochemiluminescence at the Cathode via Single-Atom Catalysts Tuned Oxygen Reduction Reaction. *J. Am. Chem. Soc.* 2022, **144:** 7741-7749.

16. Xu W, Wu Y, Wang X, Qin Y, Wang H, Luo Z, *et al.* Bioinspired Single-Atom Sites Enable Efficient Oxygen Activation for Switching Anodic/Cathodic Electrochemiluminescence. *Angew. Chem. Int. Ed.* 2023, **62:** e202304625.

17. Zhou Y, Wu Y, Luo Z, Ling L, Xi M, Li J, *et al.* Regulating Reactive Oxygen Species over M-N-C Single-Atom Catalysts for Potential-Resolved Electrochemiluminescence. *J. Am. Chem. Soc.* 2024, **146:** 12197-12205.

18. Li Y, Zhao G, An B, Xu K, Wu D, Ren X, *et al.* Multimetal-Based Metal-Organic Framework System for the Sensitive Detection of Heart-Type Fatty Acid Binding Protein in Electrochemiluminescence Immunoassay. *Anal. Chem.* 2024, **96:** 4067-4075.

19. Zhao G, Wang Y, Li X, Yue Q, Dong X, Du B, *et al.* Dual-Quenching Electrochemiluminescence Strategy Based on Three-Dimensional Metal−Organic Frameworks for Ultrasensitive Detection of Amyloid-β. *Anal. Chem.* 2019, **91:** 1989-1996.

20. Zhou Z, Shang Q, Shen Y, Zhang L, Zhang Y, Lv Y, *et al.* Chemically Modulated Carbon Nitride Nanosheets for Highly Selective Electrochemiluminescent Detection of Multiple Metal-ions. *Anal. Chem.* 2016, **88:** 6004-6010.

21. Ran L, Chen Y, Zhu Y, Cai H, Pang H, Yan D, *et al.* Covalent Organic Frameworks Based Photoenzymatic Nano-reactor for Asymmetric Dynamic Kinetic Resolution of Secondary Amines. *Angew. Chem. Int. Ed.* 2024, **63:** e202319732.

22. Shi X, Wen Z, Gu Q, Jiao L, Jiang H.-L, Lv H, *et al.* Metal-support frontier orbital interactions in single-atom catalysis. *Nature* 2025, **640:** 668-675.

23. Spivey T, Holewinski A. Selective Interactions between Free-Atom-like d-States in Single Atom Alloy Catalysts and Near-Frontier Molecular Orbitals. *J. Am. Chem. Soc.* 2021, **143:** 11897-11902.

24. Shao P, Ren Z, Zhao B, Wang X, Li J, Xie J, *et al.* Theory-Guided Design of N-Confused Porphyrinic Covalent Organic Frameworks for Oxygen Reduction Reaction. *J. Am. Chem. Soc.* 2025, **147:** 8769-8777.

25. Hou H, Wu Y, Wan J, Luo R, Wu L, Zhao Y, *et al.* p-π Conjugation-Promoted Electrochemiluminescence of Halogenated Covalent Organic Framework Nanoemitters. *Angew. Chem. Int. Ed.* 2025, **64:** e202506309.

26. Xu H, Luo R, Lv H, Liu T, Liao Q, Wang Y, *et al.* Deciphering a volcano-shaped relationship between radical stability and reticular electrochemiluminescence. *Nat. Commun.* 2025, **16:** 1924.

27. Zhu C, Gong C, Cao D, Ma L. L, Liu D, Zhang L, *et al.* Cobalt-Metalated 1D Perylene Diimide Carbon-Organic Framework for Enhanced Photocatalytic α-C(sp^3)─H Activation and CO_2 Reduction. *Angew. Chem. Int. Ed.* 2025, **64:** e202504348.

28. Han Z, Zhang Y, Wu Y, Li Z, Bai L, Huo S, *et al.* Substituent-Induced Aggregated State Electrochemiluminescence of Tetraphenylethene Derivatives. *Anal. Chem.* 2019, **91:** 8676-8682.

29. Wu R, Cao Y, Liu Y, Zhou Y, Chen Z, Zhu J.-J. Alkynyl Ligands Templated Assemblies of Silver Nanoclusters with Exceptional Electrochemiluminescence Activity for Pancreatic Cancer Specific tsRNAs Measurement. *Anal. Chem.* 2024, **96:** 19396-19403.

30. Xie R, Li K, Tian R, Lu C. Spotting d-band centers of single-atom catalysts by oxygen intermediate-boosted electrochemiluminescence. *Chem. Sci.* 2024, **15:** 18085-18092.

31. Du X, Ji H, Xu Y, Du S, Feng Z, Dong B, *et al.* Covalent organic framework without cocatalyst loading for efficient photocatalytic sacrificial hydrogen production from water. *Nat. Commun.* 2025, **16:** 3024.

32. Shuang Y, Zhang Y, Wang H, Li L, Hao X, Ma Z, *et al.* Proton-Mediated Topological Interlayer Shift in 2D Covalent Organic Frameworks for Efficient Photocatalysis. *Adv. Mater.* 2025, **37:** 2500468.

33. Chen L, Chen G, Gong C, Zhang Y, Xing Z, Li J, *et al.* Low-valence platinum single atoms in sulfurcontaining covalent organic frameworks for photocatalytic hydrogen evolution. *Nat. Commun.* 2024, **15:** 10501.

34. Fu P, Chen C, Wu C, Meng B, Yue Q, Chen T, *et al.* Covalent Organic Framework Stabilized Single CoN_4Cl_2 Site Boosts Photocatalytic CO_2 Reduction into Tunable Syngas. *Angew. Chem. Int. Ed.* 2024, **64:** e202415202.

35. Chi M, Zhao J, Ke J, Liu Y, Wang R, Wang C, *et al.* Bipyridine-Confined Silver Single-Atom Catalysts Facilitate In-Plane C-O Coupling for Propylene Electrooxidation. *Nano Lett.* 2024, **24:** 1801-1807.

36. Jiang X. H, Zhang L. S, Liu H. Y, Wu D. S, Wu F. Y, Tian L, *et al.* Silver Single Atom in Carbon Nitride Catalyst for Highly Efficient Photocatalytic Hydrogen Evolution. *Angew. Chem. Int. Ed.* 2020, **59:** 23112-23116.

37. Fang L, Qiu S, Xu H, Ye T, Li L. Encapsulation of Single-Atoms into Covalent Organic Frameworks for Highly Efficient and Persistent H_2O_2 Photosynthesis via Biphasic Flow Chemistry. *Adv. Funct. Mater.* 2025, **35:** 2504676.

38. Ran L, Li Z. W, Ran B, Cao J. Q, Zhao Y, Shao T, *et al.* Engineering Single-Atom Active Sites on Covalent Organic Frameworks for Boosting CO_2 Photoreduction. *J. Am. Chem. Soc.* 2022, **144:** 17097-17109.

39. He T, Zhao Z, Liu R, Liu X, Ni B, Wei Y, *et al.* Porphyrin-Based Covalent Organic Frameworks Anchoring Au Single Atoms for Photocatalytic Nitrogen Fixation. *J. Am. Chem. Soc.* 2023, **145:** 6057-6066.

40. Wong J. M, Zhang R, Xie P, Yang L, Zhang M, Zhou R, *et al.* Revealing Crystallization-Induced Blue-Shift Emission of a Di-Boron Complex by Enhanced Photoluminescence and Electrochemiluminescence. *Angew. Chem. Int. Ed.* 2020, **59:** 17461.

41. Gao N, Ren G, Zhang M, Mao L. Electroless Deposition of Palladium Nanoparticles on Graphdiyne Boosts Electrochemiluminescence. *J. Am. Chem. Soc.* 2024, **146:** 3836-3843.

42. Lu B, Guo L, Wu F, Peng Y, Lu J. E, Smart T. J, *et al.* Ruthenium atomically dispersed in carbon outperforms platinum toward hydrogen evolution in alkaline media. *Nat. Commun.* 2019, **10:** 631.

43. Xu W, Wu Y, Yu X, Wang H, Qin Y, Yang W, *et al.* Ru-OH-Zr Site over Metal-Organic Frameworks Boosts Coreactant Activation for Efficient Electrochemiluminescence. *Nano Lett.* 2024, **25:** 276-283.

44. Wang Y, Jiang D, Bian Y, Du X, Shan X, Wang W, *et al.* Self-Photocatalysis Boosted Electrochemiluminescence System of Pyrene Based Hydrogen-Bonded Organic Framework: Oxygen-Vacancy Mediated Adsorption and Peroxydisulfate Radical Activation. *Adv. Funct. Mater.* 2024, **35:** 2417733.

45. Han D, Sojic N, Jiang D. Spatial Profiling of Multiple Enzymatic Activities at Single Tissue Sections via Fenton-Promoted Electrochemiluminescence. *J. Am. Chem. Soc.* 2025, **147:** 9610-9619.

46. Li C. P, Yang Z, Wang J, Cheng H, Liu J. X, Ding Y. J, *et al.* Nanoconfinement-Enhanced Aggregation-Induced Electrochemiluminescence for Smartphone-Adopted Imaging Analysis of cTnI. *Adv. Funct. Mater.* 2025, **35:** 2504380.

47. Nie Y, Tao X, Zhou Y, Yuan X, Zhuo Y, Chai Y, *et al.* Kill Three Birds with One Stone: Poly(3,4-ethylenedioxythiophene)-Hosted Ag Nanoclusters with Boosted Cathodic Electrochemiluminescence for Biosensing Application. *Anal. Chem.* 2020, **93:** 1120-1125.

48. Chen X, Su J, Xiang D, Yuan Z, Lu C. Rapid Size Determination of Quasispherical Gold Nanoparticles by Electrocatalysis Efficiency-Regulated Electrochemiluminescence. *Anal. Chem.* 2024, **96:** 17689-17697.

49. Wu T, Liu G, Zhang Z, Cai X, Liu H, Dong P, *et al.* Facet Engineering-Modulated Electrochemiluminescence of Reticular Crystalline Nanoemitters. *Small* 2025, **21:** e07636.

50. Li H, Lu Q, Shi J, Zhang X, Sun P, Yan X, *et al.* Enzyme-Engineered Metal-Organic Frameworks for the Construction of Organophosphorus Pesticide Biosensor. *Adv. Funct. Mater.* 2023, **34:** 2309383.

51. Xi M, Wu Y, Li J, Wang H, Qin Y, Wang C, *et al.* Pre-Adsorbed H-Mediated Electrochemiluminescence. *Nano Lett.* 2024, **24:** 8809-8817.

52. Grimme S, Antony J, Ehrlich S, Krieg H. A consistent and accurate ab initio parametrization of density functional dispersion correction (DFT-D) for the 94 elements H-Pu. *J. Chem. Phys.* 2010, **132:** 154104.

53. Li W, Long R, Tang J, Prezhdo O. Influence of Defects on Excited-State Dynamics in Lead Halide Perovskites: Time-Domain ab Initio Studies. *J. Phys. Chem. Lett.* 2019, **10:** 3788-3804.

Acknowledgments

The authors gratefully acknowledge the Analytical and Testing Center, College of Chemistry, Central China Normal University, for their assistance with the testing services.

Funding

C.Z. discloses support for the research of this work from the National Natural Science Foundation of China [grant number 22374054], the Fundamental Research Funds for the Central Universities [grant number CCNU25QN004 and CCNU24JCPT032] and the Program of Introducing Talents of Discipline to Universities of China [grant number 111 program, B17019]. L.H. discloses support for the research of this work from the National Natural Science Foundation of China [grant number 22474103].

Author contributions

H.W.: investigation, data curation, writing-original draft. Y.D.: providing help in measurements. J.H.: providing help in measurements. Y.C.: providing help in free energy calculations. J.L.: providing help in result interpretation. Y.Q.: formal analysis. R.L.: validation. L.H.: conceptualization, writing-review & editing. W.G.: methodology, formal analysis. H.Y.: validation. C.Z.: supervision, conceptualization, funding acquisition, writing-review & editing.

Competing interests

The authors declare no competing interests.

Figure captions

Fig. 1 | Design principles of this work. Challenges in the design of ECL-active COFs and the design principle of metal single atom-enhanced ECL performance of COFs in this work.

Fig. 2 | Schematic synthesis of M/PP-COF and preliminary DFT-based screening. a Illustrations for the structure and synthesis of PP-COF and M/PP-COF. **b** Frontier orbital coupling diagrams and energy-aligned LUMO positions of PP-COF with various metal atoms (M = Fe, Co, Ni, Pt, Cu, Ag, Au). **c** The HOMO and LUMO distributions of PP-COF and Ag/PP-COF, where Ag is calculated with a d^{10} electron configuration. **d** The change in the charge of the N atom in phenanthroline after coordination with different metal centers. **e** The density of states of Ag/PP-COF and Au/PP-COF.

Fig. 3 | Structure characterization of PP-COF and Ag_{SA}/PP-COF. a FTIR spectra, **b** ^{13}C ss-NMR spectra of PP-COF. **c** PXRD patterns of PP-COF and Ag_{SA}/PP-COF. **d** TEM image of Ag_{SA}/PP-COF (inset shows the corresponding HRTEM image). **e** HAADF and corresponding elemental mapping of C, N, O, and Ag of Ag_{SA}/PP-COF. **f** AC-HAADF-STEM images of Ag_{SA}/PP-COF. Inset: corresponding intensity profile of grayscales. **g** Ag 3*d* XPS spectra, **h** N 1*s* XPS spectrum of PP-COF and Ag_{SA}/PP-COF. **i** N_2 adsorption-desorption isotherms of PP-COF and Ag_{SA}/PP-COF.

Fig. 4 | ECL and electrochemical properties of PP-COF and M/PP-COF. a ECL intensity and CV curve of PP-COF and Ag_{SA}/PP-COF in 0.1 M PBS with 0.1 M $K_2S_2O_8$ under air conditions (potential range: from 0 V to -1.8 V; scan rate: 0.1 V s^{-1}). **b** Comparison of ECL intensity between PP-COF and M/PP-COFs (M = Cu, Au, Pt, Fe, Co, Ni) (Data are represented as mean ± SD, n = 3). **c** ECL intensity of Ag_{SA}/PP-COF before and after S^{2-} poisoning. **d** Tafel slopes of PP-COF and Ag_{SA}/PP-COF. **e** Bode plots for $K_2S_2O_8$ activation induced by Ag_{SA}/PP-COF at different applied potentials. **f** Time-dependent ECL intensity of PP-COF and Ag_{SA}/PP-COF.

Fig. 5 | Mechanistic study of Ag_{SA} enhanced ECL of PP-COF. a Inhibited activity of Ag_{SA}/PP-COF after treatment with various concentrations of scavengers, including IPA and TBA (Data are represented as mean ± SD, n = 3). **b** *In situ* electrical EPR spectra in the presence of $K_2S_2O_8$ and DMPO (-1.8 V). [DMPO-OH]•: blue star; [DMPO-SO_4]•: green diamond. **c** Double potential step chronocoulometry curves of $K_2S_2O_8$ on Ag_{SA}/PP-COF: Q_f-$t^{1/2}$ and $|Q_r|$-$f(t)$ plots, pulse width: 0.25 s (Q_f and Q_r represent the forward and reverse stepwise charge transfers, respectively.). **d e** *In situ* FTIR spectra of PP-COF (blue) and Ag_{SA}/PP-COF (red) at various applied potentials from -0.1 V to -1.8 V. **f** Mechanistic illustration of $K_2S_2O_8$ reduction pathways on PP-COF and Ag_{SA}/PP-COF with associated free-energy diagrams.

Fig. 6 | Ag_{SA}/PP-COF-based OPs sensor. a Schematic diagram of the Ag_{SA}/PP-COF-based ECL sensing mechanism. **b** ECL kinetic curves, **c** linear correlation of the proposed ECL detection platform for OPs (OPs concentration: 0.1, 0.5, 1, 10, 100, and 1000 ng mL^{-1}) (Data are represented as mean ± SD, n = 3). **d** Selectivity test, **e** stability test, **f** reproducibility test of OPs detection (Data are represented as mean ± SD, n = 3).

Editorial summary:

The incorporation of metal single-atom into covalent organic frameworks facilitates co-reactant activation and charge transport enhancing electrochemiluminescence, however, can also trigger intramolecular electron transfer quenching that degrades the electrochemiluminescence efficiency. Here the authors achieved the coordination of silver atom into pyrene phenanthroline covalent organic frameworks, breaking the catalysis-quenching dilemma of metals and thereby achieving enhanced electrochemiluminescence performance.

Peer review information: *Nature Communications* thanks the anonymous reviewers for their contribution to the peer review of this work. A peer review file is available.

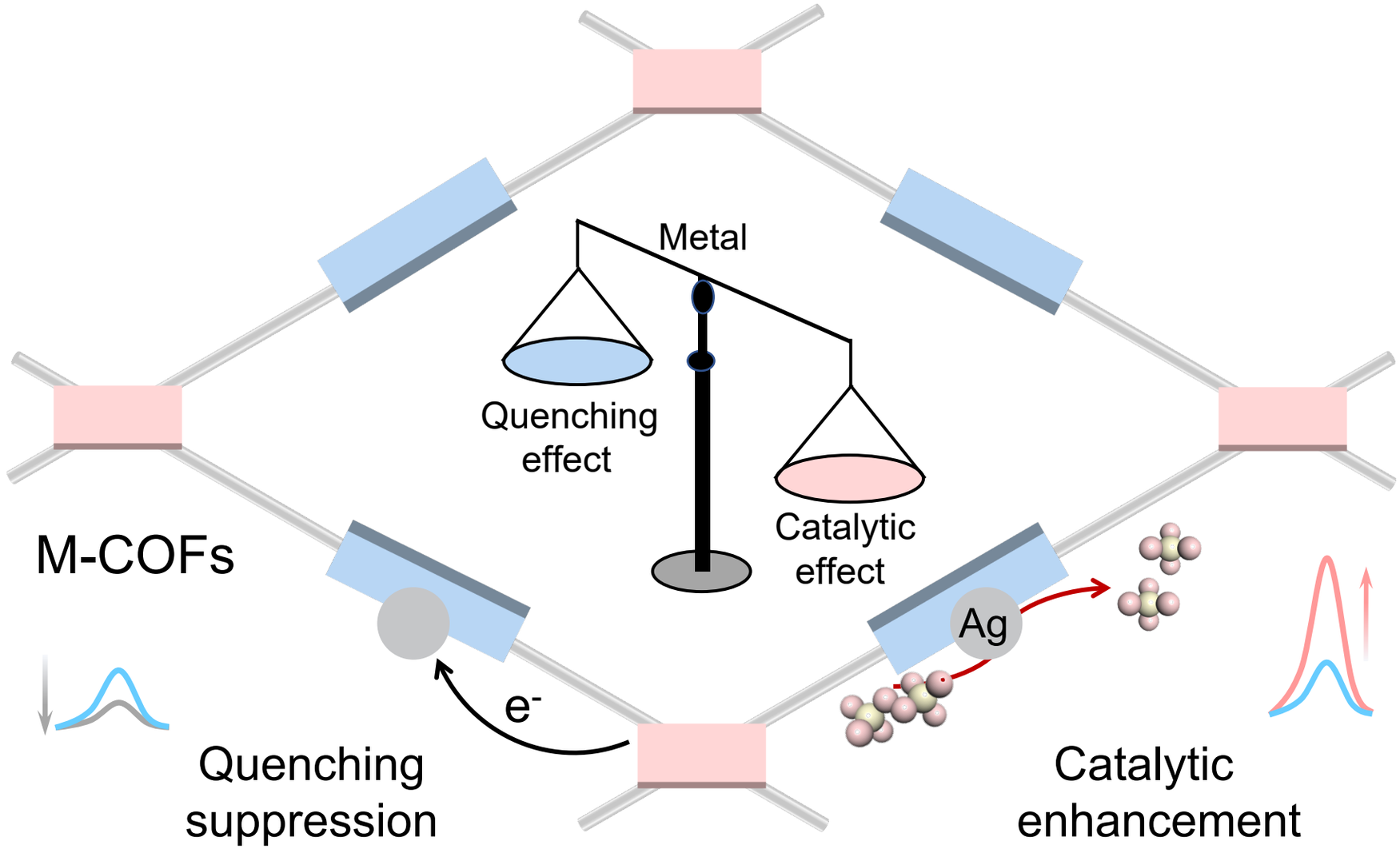
Metal
Quenching effect
Catalytic effect
M-COFs
e-
Ag
Quenching suppression
Catalytic enhancement

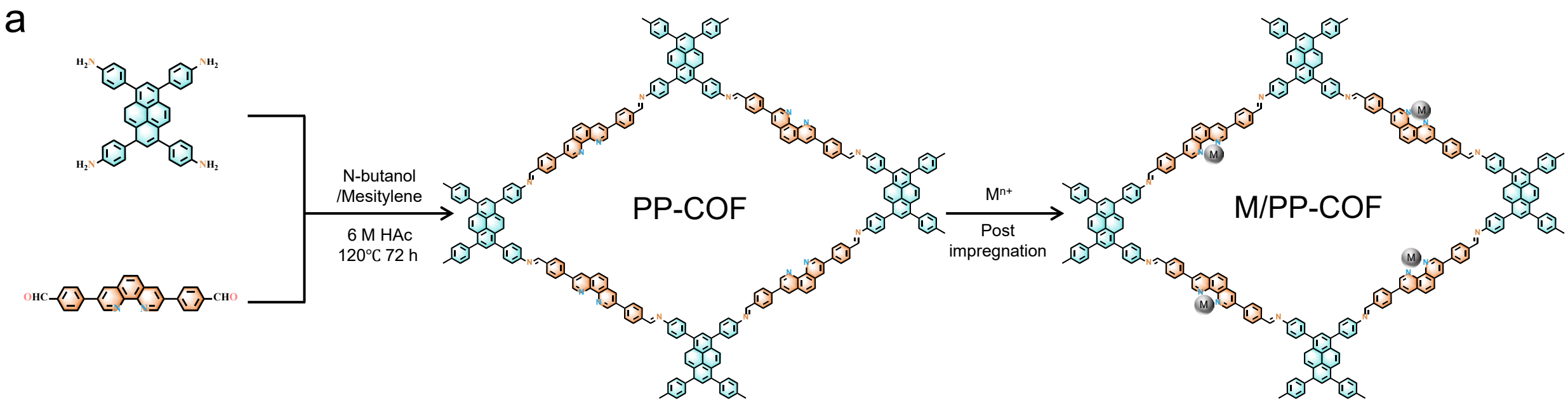
a
N-butanol
/Mesitylene
6 M HAc
120℃ 72 h
PP-COF
Mⁿ⁺
Post
impregnation
M/PP-COF

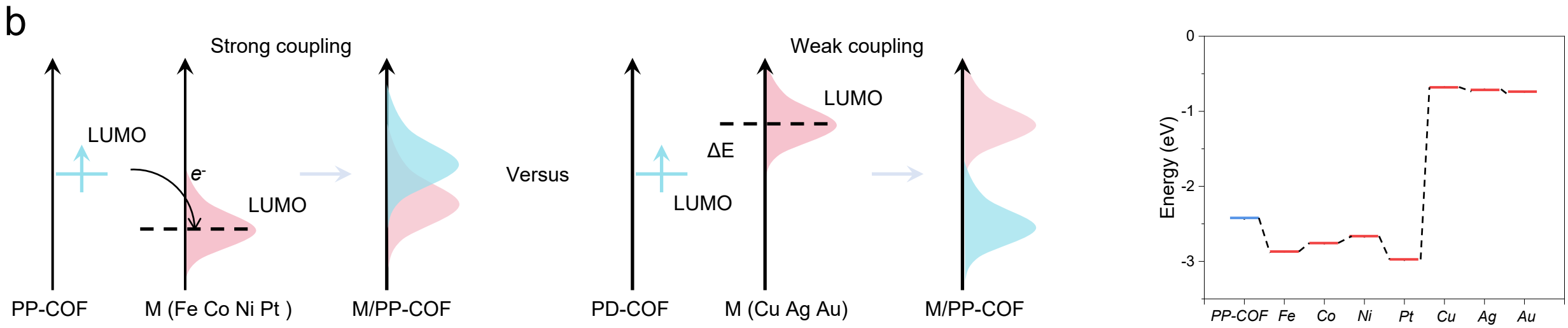
b
Strong coupling
LUMO
e⁻
LUMO
PP-COF
M (Fe Co Ni Pt)
M/PP-COF
Versus
Weak coupling
LUMO
ΔE
LUMO
PD-COF
M (Cu Ag Au)
M/PP-COF
Energy (eV)
0
-1
-2
-3
PP-COF
Fe
Co
Ni
Pt
Cu
Ag
Au

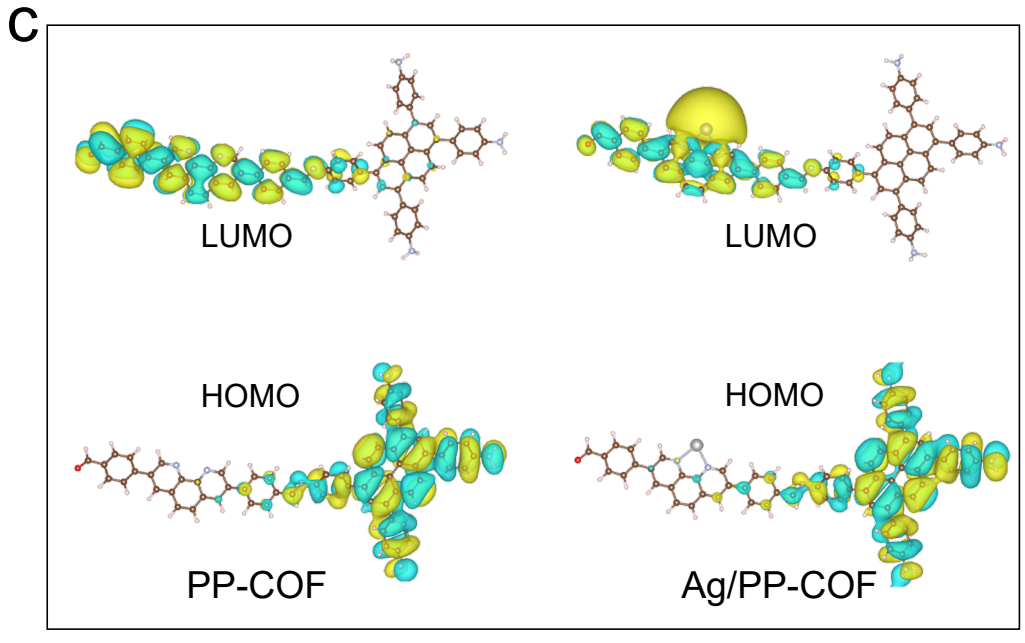
c
LUMO
LUMO
HOMO
HOMO
PP-COF
Ag/PP-COF

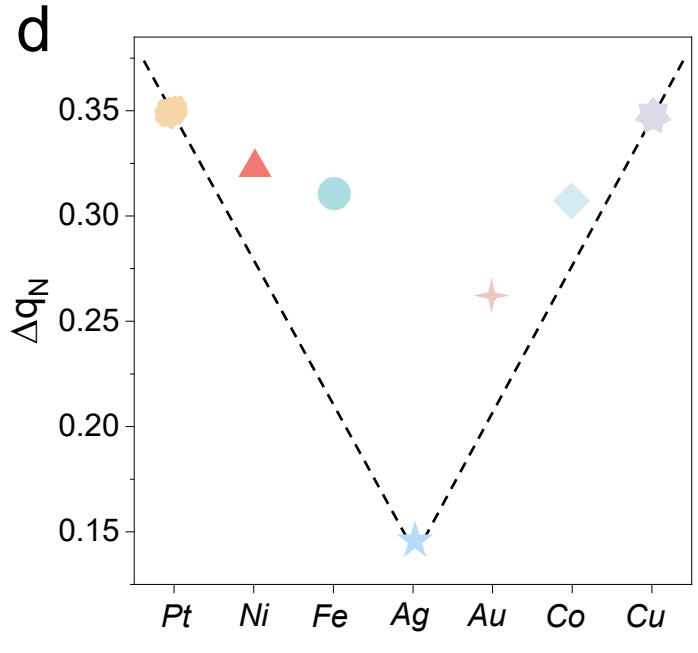
d
ΔqN
0.35
0.30
0.25
0.20
0.15
Pt
Ni
Fe
Ag
Au
Co
Cu

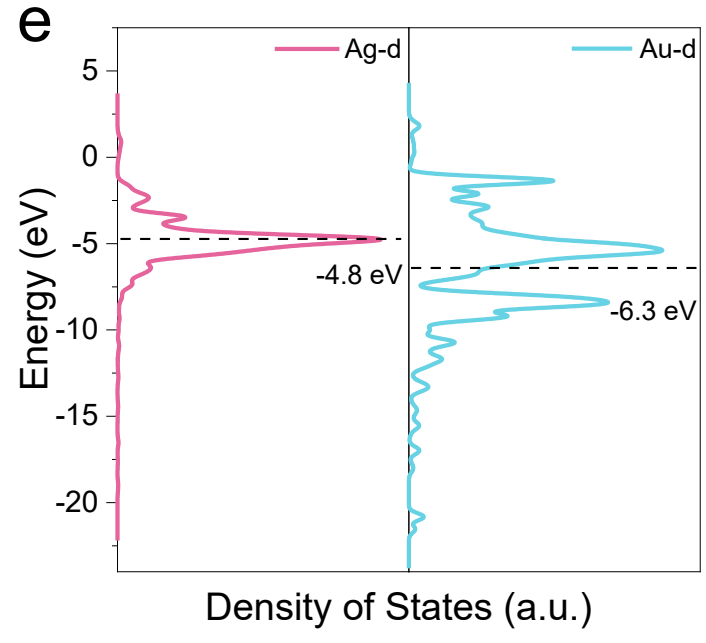
e
Ag-d
Au-d
Energy (eV)
5
0
-5
-10
-15
-20
-4.8 eV
-6.3 eV
Density of States (a.u.)

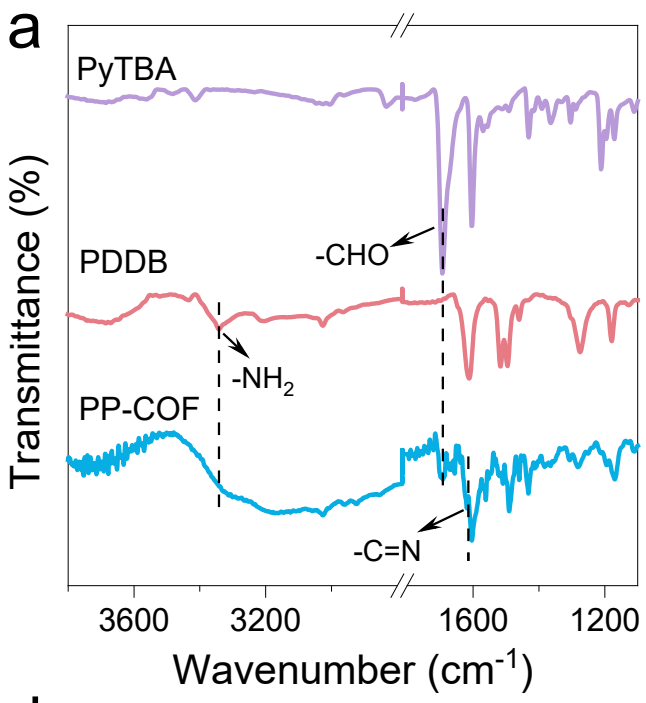
a
PyTBA
PDDB
PP-COF
-CHO
-NH2
-C=N
Transmittance (%)
3600
3200
1600
1200
Wavenumber (cm-1)

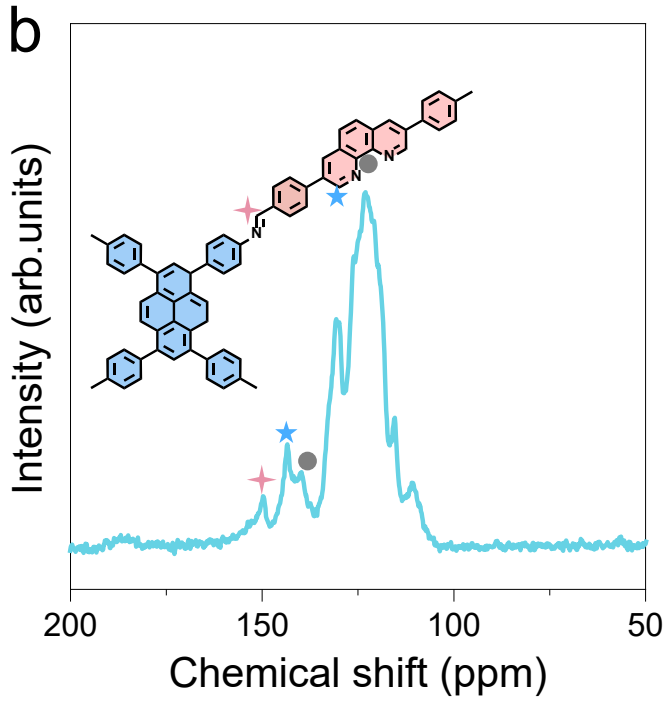
b
Intensity (arb.units)
200
150
100
50
Chemical shift (ppm)

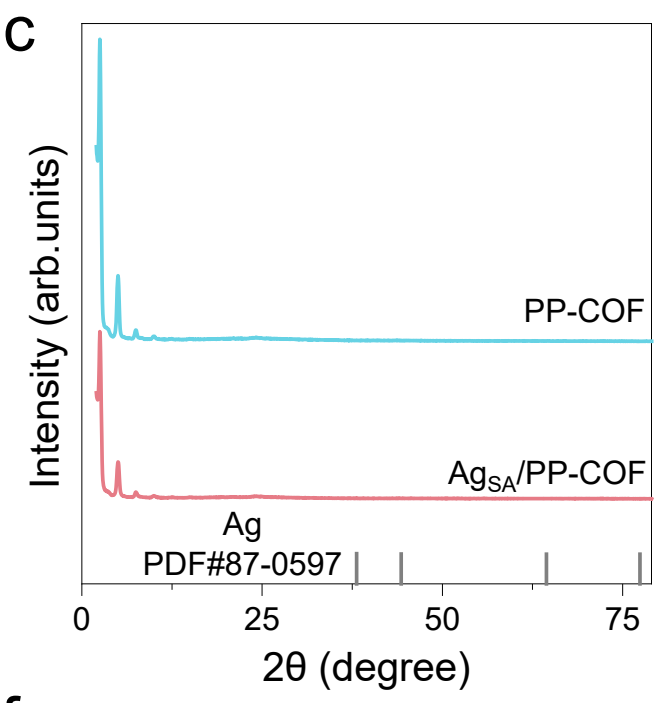
c
Intensity (arb.units)
PP-COF
AgSA/PP-COF
Ag
PDF#87-0597
0
25
50
75
2θ (degree)

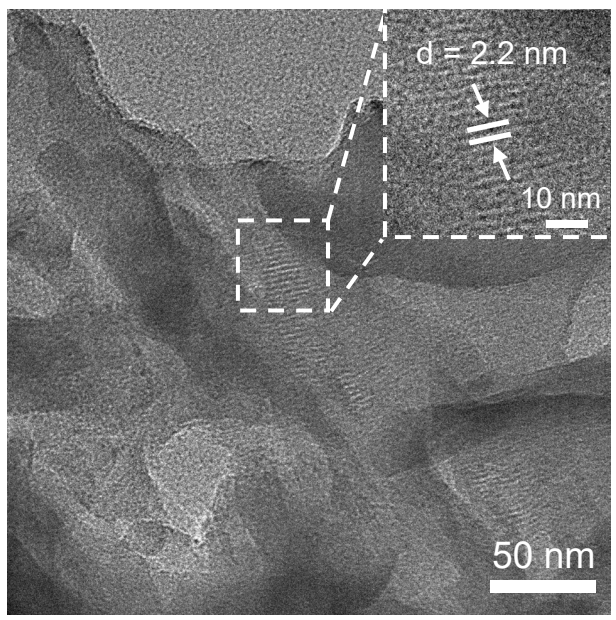
d
d = 2.2 nm
10 nm
50 nm

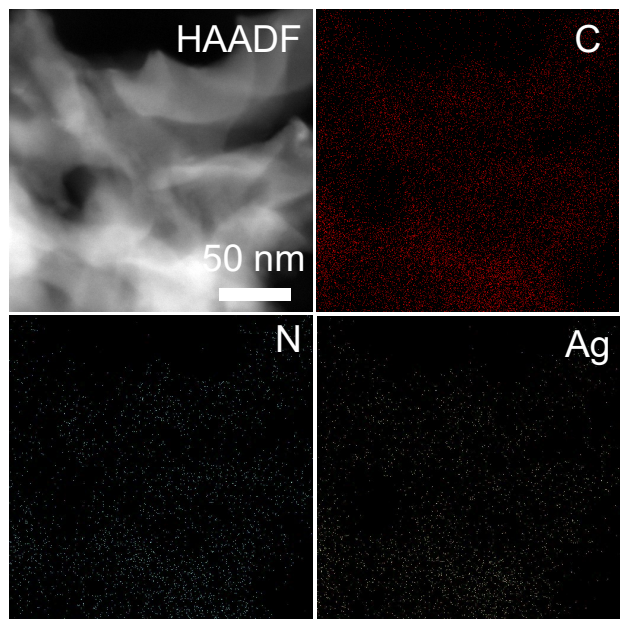
e
HAADF
C
50 nm
N
Ag

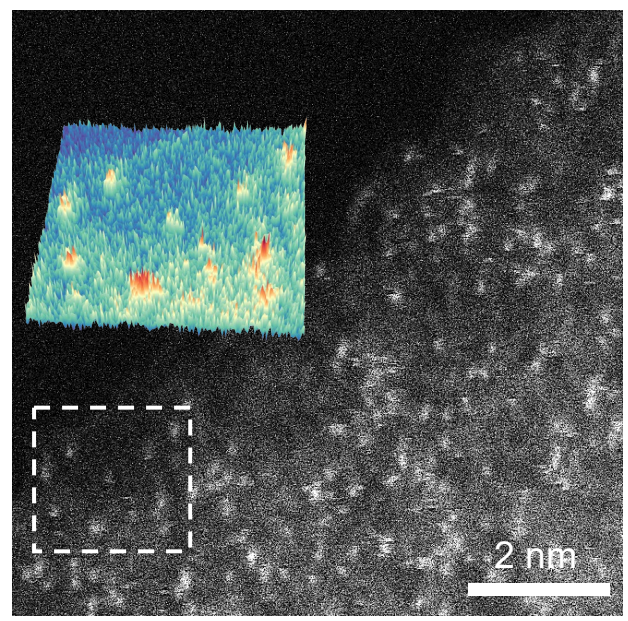
f
2 nm

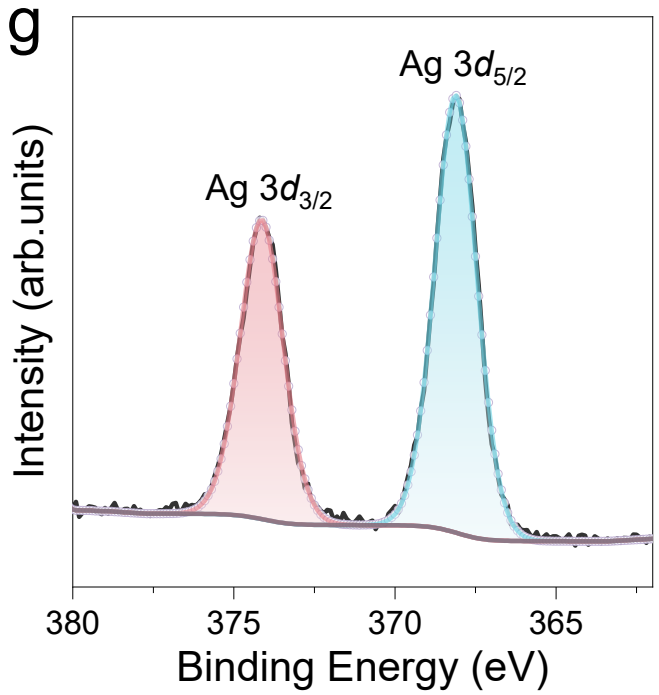
g
Ag 3d5/2
Ag 3d3/2
Intensity (arb.units)
380
375
370
365
Binding Energy (eV)

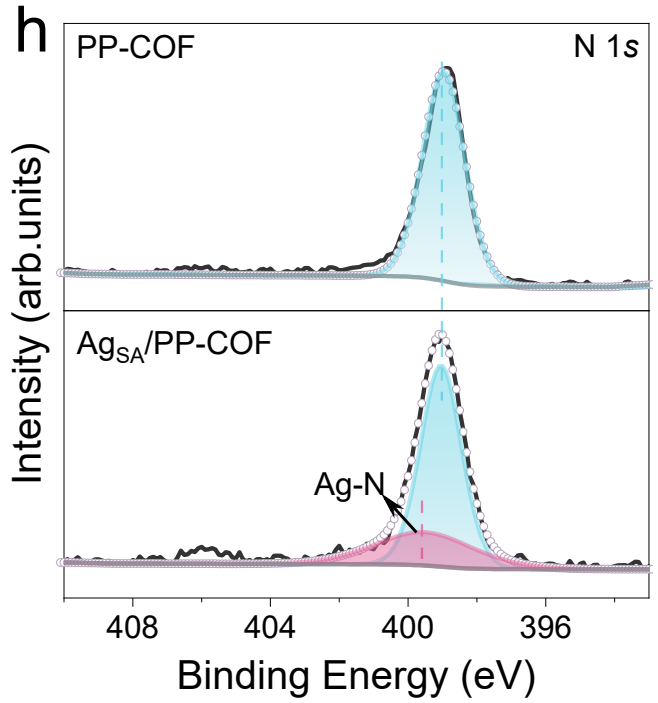
h
PP-COF
N 1s
AgSA/PP-COF
Ag-N
Intensity (arb.units)
408
404
400
396
Binding Energy (eV)

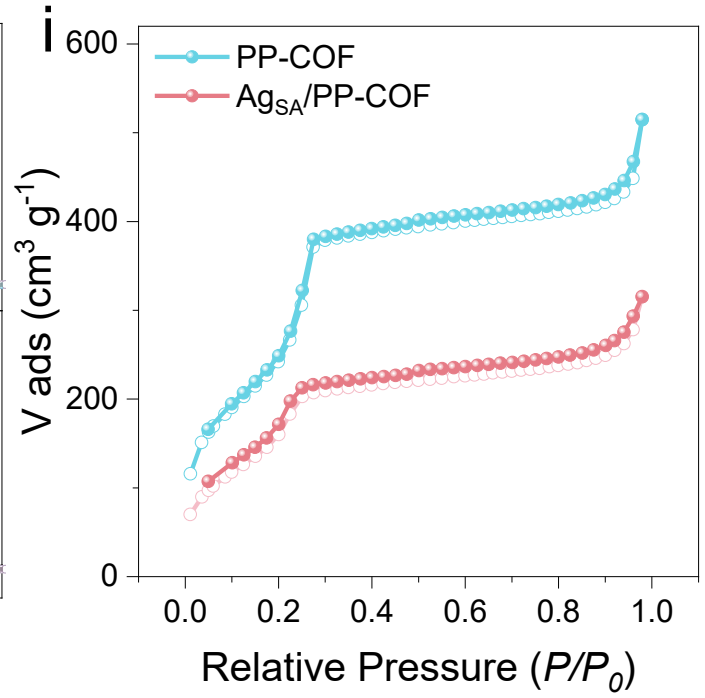
i
PP-COF
AgSA/PP-COF
V ads (cm3 g-1)
600
400
200
0
0.0
0.2
0.4
0.6
0.8
1.0
Relative Pressure (P/P0)

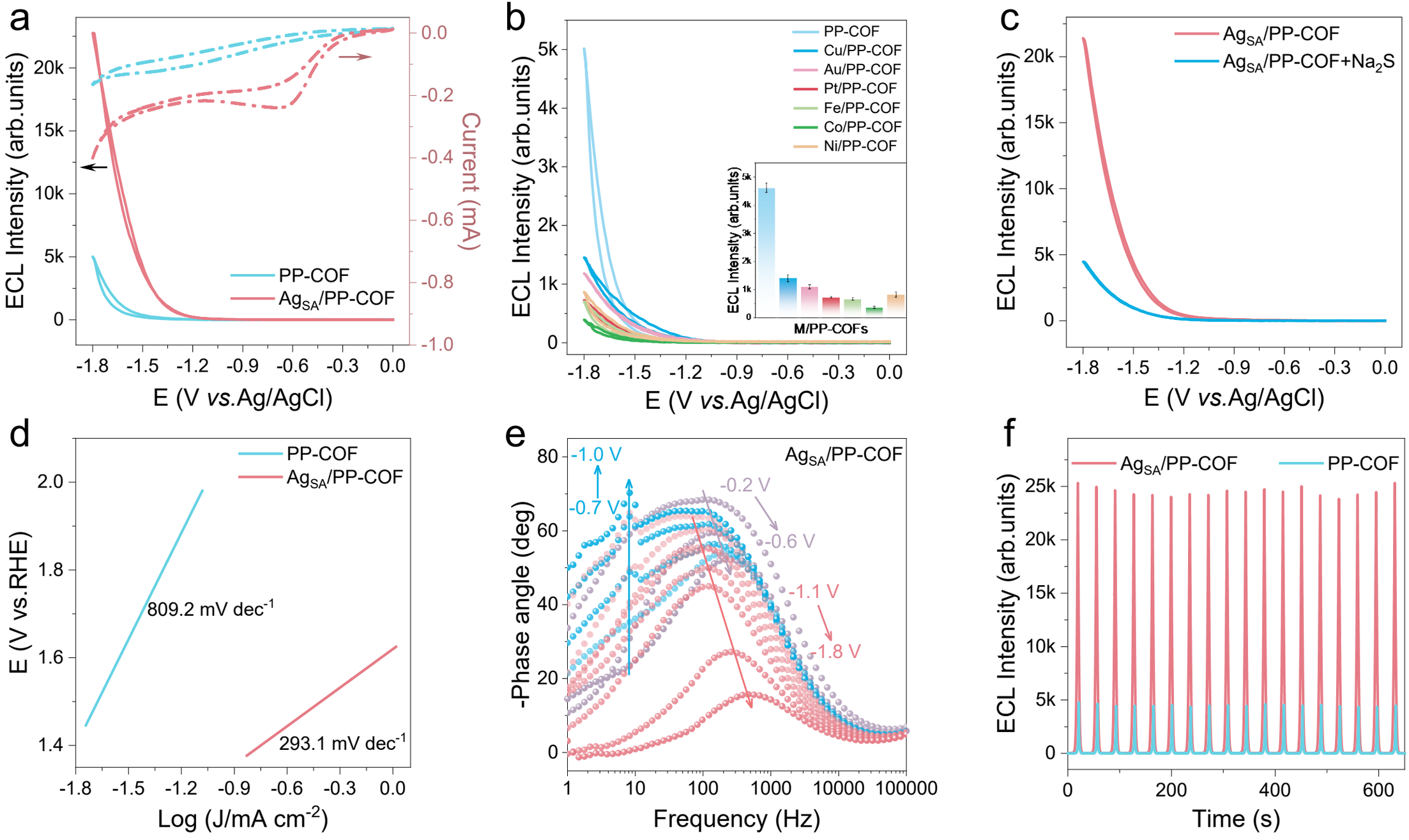
a
ECL Intensity (arb.units)
Current (mA)
E (V vs.Ag/AgCl)
PP-COF
Ag$_{SA}$/PP-COF
b
ECL Intensity (arb.units)
E (V vs.Ag/AgCl)
PP-COF
Cu/PP-COF
Au/PP-COF
Pt/PP-COF
Fe/PP-COF
Co/PP-COF
Ni/PP-COF
ECL Intensity (arb.units)
M/PP-COFs
c
ECL Intensity (arb.units)
E (V vs.Ag/AgCl)
Ag$_{SA}$/PP-COF
Ag$_{SA}$/PP-COF+Na$_2$S
d
E (V vs.RHE)
Log (J/mA cm^{-2})
PP-COF
Ag$_{SA}$/PP-COF
809.2 mV dec^{-1}
293.1 mV dec^{-1}
e
-Phase angle (deg)
Frequency (Hz)
Ag$_{SA}$/PP-COF
-1.0 V
-0.7 V
-0.2 V
-0.6 V
-1.1 V
-1.8 V
f
ECL Intensity (arb.units)
Time (s)
Ag$_{SA}$/PP-COF
PP-COF

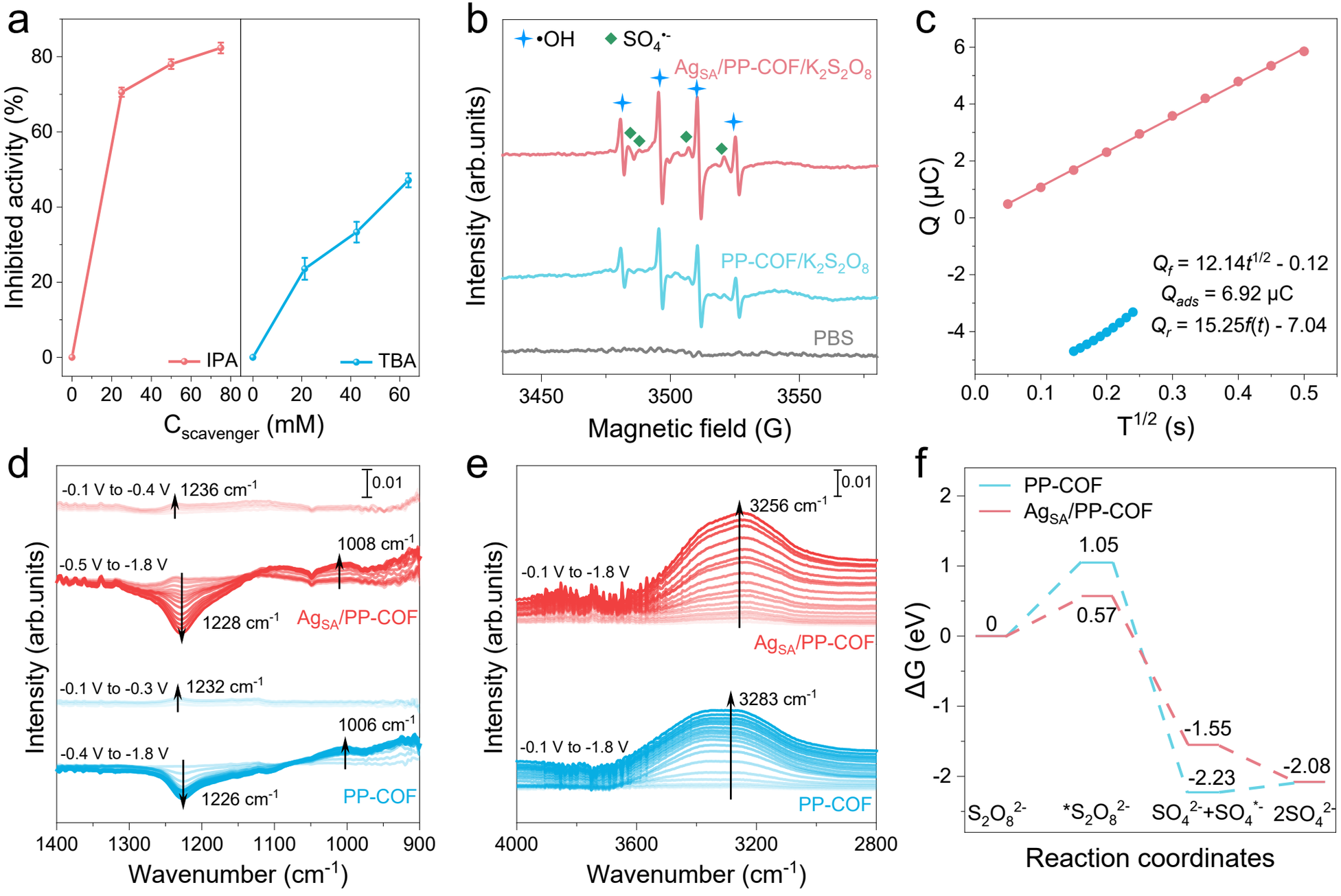
a
Inhibited activity (%)
IPA
TBA
C scavenger (mM)
b
•OH
SO4•-
AgSA/PP-COF/K2S2O8
PP-COF/K2S2O8
PBS
Intensity (arb.units)
Magnetic field (G)
c
Q (μC)
Qf = 12.14t1/2 - 0.12
Qads = 6.92 μC
Qr = 15.25f(t) - 7.04
T1/2 (s)
d
-0.1 V to -0.4 V
1236 cm-1
0.01
1008 cm-1
-0.5 V to -1.8 V
1228 cm-1
AgSA/PP-COF
-0.1 V to -0.3 V
1232 cm-1
1006 cm-1
-0.4 V to -1.8 V
1226 cm-1
PP-COF
Intensity (arb.units)
Wavenumber (cm-1)
e
3256 cm-1
0.01
-0.1 V to -1.8 V
AgSA/PP-COF
3283 cm-1
-0.1 V to -1.8 V
PP-COF
Intensity (arb.units)
Wavenumber (cm-1)
f
PP-COF
AgSA/PP-COF
1.05
0.57
0
-1.55
-2.23
-2.08
ΔG (eV)
S2O8 2-
*S2O8 2-
SO4 2-+SO4 *-
2SO4 2-
Reaction coordinates

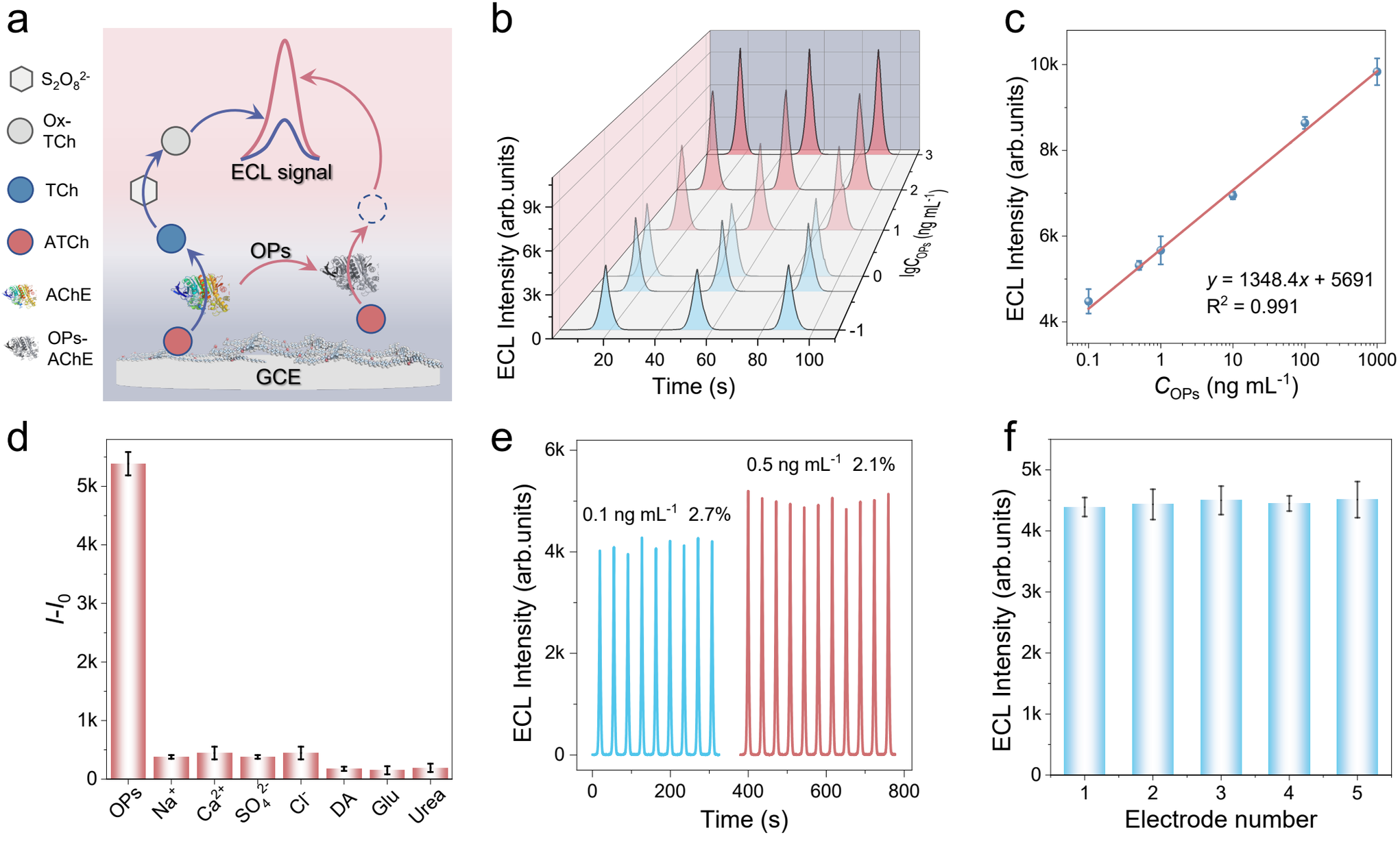
a
$S_2O_8^{2-}$
Ox-TCh
TCh
ATCh
AChE
OPs-AChE
ECL signal
OPs
GCE
b
ECL Intensity (arb.units)
Time (s)
lgC$_{OPs}$ (ng mL^{-1})
c
ECL Intensity (arb.units)
C_{OPs} (ng mL^{-1})
y = 1348.4x + 5691
R^2 = 0.991
d
I-I$_0$
OPs
Na$^+$
Ca^{2+}
SO$_4^{2-}$
Cl$^-$
DA
Glu
Urea
e
ECL Intensity (arb.units)
Time (s)
0.1 ng mL^{-1} 2.7%
0.5 ng mL^{-1} 2.1%
f
ECL Intensity (arb.units)
Electrode number